Implementation and Evaluation of a Double-Plume Convective Parameterization in NCAR CAM5

WENCHAO CHU,[a] YANLUAN LIN,[a] AND MING ZHAO[b]

[a] *Department of Earth System Science, Ministry of Education Key Laboratory for Earth System Modeling, Institute for Global Change Studies, Tsinghua University, Beijing, China*
[b] *NOAA/GFDL, Princeton, New Jersey*

(Manuscript received 4 April 2021, in final form 20 October 2021)

ABSTRACT: Performance of global climate models (GCMs) is strongly affected by the cumulus parameterization (CP) used. Similar to the approach in GFDL AM4, a double-plume CP, which unifies the deep and shallow convection in one framework, is implemented and tested in the NCAR Community Atmospheric Model version 5 (CAM5). Based on the University of Washington (UW) shallow convection scheme, an additional plume was added to represent the deep convection. The shallow and deep plumes share the same cloud model, but use different triggers, fractional mixing rates, and closures. The scheme was tested in single-column, short-term hindcast, and AMIP simulations. Compared with the default combination of the Zhang–McFarlane scheme and UW scheme in CAM5, the new scheme tends to produce a top-heavy mass flux profile during the active monsoon period in the single-column simulations. The scheme increases the intensity of tropical precipitation, closer to TRMM observations. The new scheme increased subtropical marine boundary layer clouds and high clouds over the deep tropics, both in better agreement with observations. Sensitivity tests indicate that regime-dependent fractional entrainment rates of the deep plume are desired to improve tropical precipitation distribution and upper troposphere temperature. This study suggests that a double-plume approach is a promising way to combine shallow and deep convections in a unified framework.

KEYWORDS: Model evaluation/performance; Climate models; Convective parameterization

1. Introduction

Cumulus convection has great impacts on the climate system via its effects on clouds and radiation, momentum, tropical circulation, and precipitation distribution (Arakawa 2004). Due to the coarse grid spacing of current global climate models (GCMs), cumulus parameterizations (CPs) are still needed to capture the statistical effects of cumulus ensemble on the model mean fields. The performance of GCM-simulated clouds, precipitation, circulation, and even tropical cyclones is significantly influenced by convection schemes (Lin et al. 2012; Yang et al. 2013; Maher et al. 2018, among others). Many studies report that different choices of convection schemes are responsible for their difference in simulated tropical cyclone intensity and precipitation (Knutson and Tuleya 2004; Zhao et al. 2012), Hadley circulation strength (Hourdin et al. 2006), and tropical transients (Slingo et al. 1994). Therefore, it is very important to reasonably represent the convective processes in GCMs.

CP development has a long history (Kuo 1965, 1974; Arakawa and Schubert 1974), but the progress has been rather slow due to its complexity (Randall et al. 2003). There are three major types of CP, including the moist adjustment scheme originated from Manabe et al. (1965) and improved by Betts and Miller (1986), the moisture convergence scheme developed by Kuo (1965, 1974), and the mass flux scheme proposed by Arakawa and Schubert (1974). At present, most GCMs use mass flux–type CPs (e.g., Walters et al. 2019; Bechtold et al. 2008; Schmidt et al. 2014; Zhao et al. 2018a; Golaz et al. 2019, among others). Some of them used a single entraining/detraining plume to represent the cumulus ensemble with parameterized entrainment and detrainment rate, while others, following Arakawa and Schubert (1974), calculated a spectrum of plumes with different entrainment and detrainment rates in order to mimic diversified convection in nature. For example, Yoshimura et al. (2015) created an ensemble of plumes by interpolating the in-cloud variables between the two traditional updrafts with prescribed minimum and maximum entrainment rates separately. Baba (2019) defined a spectrum of plumes with different cloud base vertical velocities associated with different entrainment rates to mimic various convective updrafts. Of course, such schemes cost more computational resources.

GCMs have various shortcomings related to convection parameterizations, such as prevalent too weak but too frequent precipitation (Dai 2006; Stephens et al. 2010; Pendergrass and Hartmann 2014), weak tropical transients, like the MJO (Lin et al. 2006), and the long-lasting double ITCZ problem (Lin 2007). For example, too weak but too frequent precipitation in CAM5 is caused by too frequently triggered deep convection (Wang and Zhang 2013). Less efficient transportation of water vapor from the boundary layer to the upper troposphere by deep convection contributed to the moisture bias in the free troposphere and the corresponding radiation and precipitation bias in CAM5 (Xie et al. 2012).

Many attempts have been taken to alleviate the above problems. One major approach is to modify the existing convection schemes. By changing the relaxed CAPE closure in the original Zhang and McFarlane (1995) scheme to dynamic CAPE (DCAPE) closure, Zhang and Mu (2005) find that the double ITCZ problem has been largely alleviated in the

Corresponding author: Yanluan Lin, yanluan@tsinghua.edu.cn

DOI: 10.1175/JCLI-D-21-0267.1

Community Climate Model version 3, with a slab ocean. Tokioka et al. (1988) increased the entrainment rate in the Arakawa–Schubert convection scheme and found that tropical transients, like the MJO, were better captured. Diurnal cycles of convection can also be better captured by altering the entrainment rate and convection trigger in a convection scheme (Stirling and Stratton 2012; Xie et al. 2019; Wang et al. 2020; Cui et al. 2021). Another way is to change the structure of convection parameterization. Examples include the eddy-diffusivity mass-flux approach proposed by Siebesma et al. (2007), which combines the turbulence with shallow convection. The unified convection scheme developed by Park (2014) aims to unify the deep convection and shallow convection.

Recently, a new convection scheme that unifies the deep and shallow convection was developed and applied in GFDL Global Atmosphere Model version 4 (AM4; Zhao et al. 2018a). Different from the conventional single bulk plume scheme, the new scheme contains two plumes, one for deep and the other for shallow, at a given time step, and thus is referred to as a double-plume scheme. The new scheme, combined with other modifications, was found to improve significantly AM4's simulations of clouds, precipitation, and radiation (Zhao et al. 2018b). One advantage of the double-plume scheme is that both deep and shallow convection can develop independently within the same environment so that the calculation sequence of deep and shallow convection is no longer a problem. The other advantage is that the same cloud model can be used for both shallow and deep convection and thus a natural transition from shallow to deep convection may be better captured (Hohenegger and Bretherton 2011). Note that a similar idea was also suggested by Mapes and Neale (2011) but with a different approach. They developed a two-plume version of the University of Washington scheme (herein the UW scheme or simply UW; Bretherton et al. 2004) in CAM5. The fractional mixing rates, source air properties, and closure of the two plumes were closely related to a nondimensional prognosed convective organization parameter ("org").

In the NCAR Community Atmospheric Model version 5 (CAM5; Neale et al. 2012), convection schemes include a shallow convection scheme of Bretherton et al. (2004) and a deep convection of Zhang and McFarlane (1995). They use very different types of cloud model: a single plume in the UW shallow convection scheme but spectrum plumes in the Zhang and McFarlane convection scheme (herein the ZM scheme or simply ZM) trigger and closure. Using two schemes for shallow and deep convection separately brought extra considerations and complexities, such as the calling sequence and aerosol activation, among others. It is also hard to capture the prevalent transition of shallow to deep convection in nature. Therefore, we aim to unify deep and shallow convection in terms of cloud model and triggers. Since UW also works well for deep convections (Hohenegger and Bretherton 2011), it is natural to replace the ZM deep convection via adding another deep plume in UW, following the idea of double-plume approach in GFDL AM4 (Zhao et al. 2018a). In addition, the buoyancy sorting method in UW has been shown to be a good way for entrainment and detrainment parameterization in convections (Zhao and Austin 2005a,b).

This study aims to implement and test a double-plume scheme in CAM5 following Zhao et al. (2018a). Details of the scheme and its implementation in CAM5 are described in section 2. Section 3 summarizes the performance of the scheme using single-column model simulations. In section 4, tropical precipitation diurnal cycle and strength are tested in short-term hindcast simulations at different horizontal resolutions. Global climate simulations and their evaluation are presented in section 5. Conclusions and discussion are in section 6.

2. Scheme description and implementation in CAM5

The NCAR Community Atmospheric Model version 5 (CAM5) includes a suite of advanced physics and dynamics (Neale et al. 2012). In CAM5, the codes of dynamical and physical processes are cleanly separated so that model developers can easily replace the original schemes with new schemes. The physical package in CAM5 includes a moist turbulence scheme of Bretherton and Park (2008) followed by moist convection schemes. After convection, cloud macrophysics (Park et al. 2014) and microphysics schemes (Morrison and Gettelman 2008) are invoked. Finally, radiation and chemical processes are considered.

Moist convections in CAM5 include a deep convection scheme of ZM and a shallow convection scheme of UW. The UW scheme aims to better represent the turbulence-driven marine subtropical shallow convections. The scheme uses a single entraining–detraining bulk plume cloud model, in which the entrainment rate is determined by a buoyancy sorting algorithm suggested by Kain and Fritsch (1990). The trigger and closure of UW is closely coupled to turbulence kinetic energy (TKE) diagnosed from planetary boundary layer (PBL) scheme and convective inhibition (Mapes 2000; Bretherton et al. 2004). The source air departs at the layer just above the top of the PBL with its total water (q_t) chosen to be the surface layer specific humidity and the virtual liquid water potential temperature (θ_{vl}) at the lowest value within the PBL. The closure is to ensure a neutral or weakly negatively buoyant updraft at the lifting condensation level (LCL). The initial velocity of the plume is determined by the mean $\overline{\text{TKE}}$ within the PBL. It assumes a Gaussian distribution of the vertical velocity at the PBL top with a mean of zero and variance linearly proportional to the $\overline{\text{TKE}}$, expressed as $\sigma_w^2 = k_f \times \overline{\text{TKE}}$. The term k_f is an empirical parameter and set to be 0.5 in Bretherton et al. (2004) but is modified to 1.0 in CAM5. Then the fraction of convection area f and cloud base mass flux M_b can be obtained as

$$f = \frac{1}{2}\text{erfc}\left(\frac{w_c}{\sqrt{2k_f \times \overline{\text{TKE}}}}\right), \tag{1}$$

$$M_b = \bar{\rho}\sqrt{\frac{k_f \times \overline{\text{TKE}}}{2\pi}}\exp\left(-\frac{w_c^2}{2k_f \times \overline{\text{TKE}}}\right), \tag{2}$$

TABLE 1. A comparison and summary of parameterization methods in UW, DP-Z, and DP-THU. Terms are as follows: q_t (kg kg^{-1}) is the total water specific humidity; θ_{il} (K) is the liquid-ice potential temperature; h_{il} is liquid-ice static energy; ε_0 (km^{-1}) is the fractional mixing rate; z (m) is the height above the surface; CRH is the average relative humidity of the free troposphere, and CRH_0 is a critical relative humidity (40%); Q_l (kg kg^{-1}) is the cloud water content; q_i (kg kg^{-1}) is the cloud ice content and $q_c = q_l + q_i$; Δp (Pa) is the pressure height of each model layer; Q_{cs} is the autoconversion threshold for shallow convection and q_{cd} is the autoconversion threshold for deep convection.

	UW	DP-Z	DP-THU
Conserved variable	q_t, θ_{il}	q_t, h_{il}	q_t, θ_{il}
Trigger	CIN-TKE	CIN-TKE shallow Relaxed-CWFN deep	CIN-TKE shallow CIN-DPCAPE deep
Closure	CIN-TKE	CIN-TKE shallow Relaxed-CWFN deep	CIN-TKE shallow DPCAPE deep
Fractional mixing rate (km^{-1})	$\varepsilon_0(z) = \frac{7}{z}$	$\varepsilon_0 = \begin{cases} 3, & \text{shallow} \\ 0.9 - 0.8 \times \frac{\mathrm{CRH} - \mathrm{CRH}_0}{1 - \mathrm{CRH}_0}, & \text{deep} \end{cases}$	$\varepsilon_0(z) = \begin{cases} 3, & \text{shallow} \\ 1.2 - \mathrm{RH}(z), & \text{deep} \end{cases}$
Microphysics	$P = \max(q_c - q_{c0}, 0)$	$P_r = 6 \times 10^{-5} \times \Delta p \times \max(q_l - q_{l0}, 0)$, $P_s = 11 \times 10^{-5} \times \Delta p \times q_i$	$P = \max(q_c - q_{cs}, 0)$ shallow, $P = \max(q_c - q_{cd}, 0)$ deep
Re-evaporation	Sundqvist (1988)	Moorthi and Suarez (1999)	Sundqvist (1988)

where w_c is the minimal vertical velocity that can overcome the convective inhibition (CIN) above the PBL, which can be written as $w_c = \sqrt{2\mathrm{CIN}}$. For a Gaussian distribution, a lower bound for f (i.e., the minimum area allowed for convection) must be set to avoid dummy convection being triggered. If f is larger than 0.001, the convective plume is identified. The trigger and closure in UW are called CIN-TKE later (Table 1).

The fractional mixing rate ε_0 of the plume is parameterized as a function of height (km) as

$$\varepsilon_0 = \frac{7}{z}. \tag{3}$$

Zhao et al. (2018b) added a deep plume into the original UW scheme to make it a double-plume scheme (referred to as DP-Z). Deep and shallow plumes are independent of each other, but they share the same cloud model with different fractional mixing rates, triggers, closures, and microphysical parameterizations. For the shallow plume, the height-dependent fractional mixing rate is replaced by a tunable constant, which is set to be 3 km^{-1}. For the deep plume, the fractional mixing rate is parameterized as a function of free troposphere mean relative humidity as

$$\varepsilon_0 = \varepsilon_1 + \frac{\zeta - \zeta_0}{1 - \zeta_0}(\varepsilon_2 - \varepsilon_1), \tag{4}$$

where ζ is the mean relative humidity of the free troposphere, ζ_0 is a critical relative humidity at 0.4, and ε_1 and ε_2 are two tunable parameters of 0.9 and 0.1 km^{-1} respectively; ε_0 is smaller in a wetter environment to roughly account for the effect of convective organization.

The trigger and closure for the shallow plume are the same as those in UW in DP-Z, but a relaxed cloud work function (CWFN) closure was used for the deep plume. CWFN is defined as a vertical integral of the buoyancy from cloud base to the level of neutral buoyancy in the plume. The DP-Z scheme relaxed CWFN to a reference value of 10 J kg^{-1} with a relaxation time scale of 8 h (Zhao et al. 2018b). The deep plume is triggered only when the CWFN is greater than 10 J kg^{-1} and mean relative humidity ζ greater than 0.4.

The parameterization of convective precipitation is also changed. In UW, convective precipitation is calculated using a Heaviside step function $H(q_c - q_{\mathrm{cr}})$, in which q_c is cloud water content and q_{cr} is a threshold of 0.7 g kg^{-1}. In the DP-Z scheme, in contrast, convective precipitation is parameterized as a function of pressure height and condensate within the plume (Table 1) with autoconversion occurring only when the cloud water content is greater than 0.2 g kg^{-1}. The deeper the vertical layer, the more precipitation will form with the same amounts of condensates in the plume.

During the implementation of the double-plume scheme in CAM5, we made several modifications, including the trigger, closure, fractional mixing rate, and detrainment process, in order to better coordinate with boundary layer turbulence scheme and macrophysics scheme in CAM5. The scheme is named DP-THU with detailed modifications described below and summarized in Table 1.

In the CAM5 physics module, ZM and UW are independent of each other and invoked by the physics package sequentially. Our strategy is to disable ZM and replace UW with the new scheme. Other relevant schemes used in CAM5 include the boundary layer scheme of Bretherton and Park (2009), the cloud macrophysics of Park (2014), and the microphysics of Morrison and Gettelman (2008; note that we used version 1.0 of their microphysics rather than version 1.5 in CESM1.2.1).

a. *Trigger function*

The trigger function is used to determine the occurrence of convection. Note that the triggering of convection can only be initiated when the boundary layer TKE can overcome the CIN (i.e., CIN-TKE, introduced above; see Table 1). Once the convection is determined to occur, whether it can develop

as a deep plume is controlled by another trigger described below.

Most schemes determine the occurrence of deep convection based on CAPE. Xie and Zhang (2000) introduced a dynamic CAPE (DCAPE) trigger, in which the convection can be triggered only when the large-scale forcing is making a positive contribution to the existing CAPE. This trigger was proved to give better performance on simulating the onset and strength of convection in Energy Exascale Earth System Model (E3SM; Xie et al. 2019) and Cui et al. (2021).

Here, following Xie and Zhang (2000), we used the DCAPE approach. Instead of using CAPE, we used the density-weighted CAPE (PCAPE), calculated as

$$\text{PCAPE} = -\int_{p_b}^{p_t} \frac{\theta_{vu} - \overline{\theta_v}}{\overline{\theta_v}} dp, \tag{5}$$

where θ_{vu} and $\overline{\theta_v}$ are the virtual potential temperature of the plume and the environment respectively. PCAPE represents the buoyancy factor integrated from the plume base p_b to the plume top p_t. The deep convection will be triggered as long as the large-scale (i.e., advection, radiation, and large-scale phase change) and PBL generation of PCAPE is greater than zero with a positive PCAPE.

We also need to determine the source air parcel properties of the plume as the initial condition for the cloud model. DP-Z directly uses the properties of environment at a certain layer, such as the maximum moist static energy layer or the surface layer, for the source air properties. It also assumes that both deep and shallow plumes depart at the same height and share the same cloud base properties. However, cloud-resolving model simulations (e.g., Baba 2019; Khairoutdinov and Randall 2002; von Salzen and McFarlane 2002) suggest that the cloud base of deep convection is generally higher with slightly larger initial vertical velocities than shallow convection in environment favorable for both deep and shallow convection. Accordingly, different from the shallow plume, we assume that the source air parcel of the deep plume has a higher temperature excess (0.5 K) to the environment at its departure level to mimic the higher cloud base of the deep plume.

The new trigger function still assumes that the source air departs at the top of PBL as UW, but its properties, namely the total water q_t and liquid-ice potential temperature θ_{il}, are set to be the mean value of the environment within the PBL. Choosing vertically averaged environment properties rather than directly using the properties of environment at a certain layer is based on two considerations. One is to avoid the spurious deep convection in the early morning hours when the surface layer undergoes strong heating (e.g., Bechtold et al. 2004). Another is to account for the impact of turbulent mixing on the source air properties within the PBL.

b. The cloud model

The cloud model is an entraining/detraining bulk plume model, used for both shallow and deep plume, but with different entrainment and detrainment specifications in DP-Z. The cloud model used in DP-THU is identical to DP-Z except for the conservation variables (Table 1). Assuming steady state, the cloud model explicitly solves the mass flux (M_u), liquid-ice potential temperature (θ_{il}), total water (q_t), and horizontal wind (u, v) of the updraft. Downdrafts are not explicitly considered. The specific humidity (q_v), liquid water content (q_l), ice water content (q_i), and virtual potential temperature (θ_v) of the updraft are diagnosed from the saturation adjustment module. The formulation of the cloud model is described as follows:

$$\frac{\partial M_u}{\partial z} = M_u(\varepsilon - \delta), \tag{6}$$

$$\frac{\partial \varphi_u}{\partial z} = \varepsilon(\bar{\varphi} - \varphi_u) + S_\varphi, \tag{7}$$

$$\frac{1}{2}\frac{\partial}{\partial z} w_u^2 = B_u - \varepsilon w_u^2 - P - D. \tag{8}$$

Equation (6) is the mass conservation equation, in which M_u is mass flux (kg m^{-2} s^{-1}). It can be expressed as $M_u = \sigma\rho w_u$, with σ the cloud fraction. The terms ε and δ are fractional entrainment and detrainment rate (m^{-1}), respectively. Equation (7) is a scalar/vector transportation equation, in which φ can be any scalars/vectors, such as θ_{il}, q_t, $\mathbf{u}$, or $\mathbf{v}$; S_φ is the source and sink term of the scalar/vector φ. The overbar means the property of environment and the subscript u means the property of the plume. Equation (8) is the vertical velocity equation. The first term on the rhs means the net buoyancy acceleration, which can be written as $B_u = g(\theta_{vu} - \overline{\theta_v}/\overline{\theta_v})$. The second, third, and last terms are the impact of entrainment, pressure perturbation, and subplume-scale variance, respectively. In general, the third term P can be represented as $P = -(1/\rho)(\overline{\partial p_c'}/\partial z) - g(\overline{p_c'}/\bar{p})$ and the last term D can be written as $D = [1/(\sigma\rho)](\partial\sigma\rho\overline{w_c'^2}/\partial z)$. The subscript c represents an average over the convection region. Note that term P is very important in Eq. (8) as it is the dominant term that offsets the buoyancy force (Jeevanjee 2017). However, P and D are very difficult to be directly calculated because they are subplume variables. We simplified Eq. (8) following Gregory (2001) as

$$\frac{1}{2}\frac{\partial}{\partial z} w_u^2 = \alpha B_u - b\varepsilon w_u^2, \tag{9}$$

where α and b are two parameters. Here, we set $\alpha = 1$ and $b = 2$, as in the UW and DP-Z schemes.

Note that the deep plume was forced to stop at the neutral buoyancy layer in ZM, but it is allowed to overshoot into the upper stable layer in DP-THU. This appears to be more consistent with observations.

c. Entrainment and detrainment

Entrainment of environment air into the plume is assumed to occur only at the lateral boundary of the plume by

turbulent mixing. Following UW, we use the buoyancy-sorting algorithm [Eq. (11)] for turbulent mixing entrainment ε_m and detrainment δ_m, but with different fractional mixing rate ε_0 for deep and shallow plumes. For the deep plume, ε_0 is a function of relative humidity (RH) at each level, expressed as

$$\varepsilon_0 = [1.2 - \mathrm{RH}(z)] \times \mathrm{rkm}, \tag{10}$$

where rkm is a tunable parameter to determine the mixing strength. When rkm is 1 km^{-1}, ε_0 is bounded between 0.2 and 1.2 km^{-1}, consistent with large-eddy simulation results (Romps 2010) and observations (e.g., Lu et al. 2012; Wagner et al. 2013), who found that the entrainment rate for deep convection is about 0.5–1 km^{-1}. Setting ε_0 to be a monotonically decreasing function of RH is to allow a larger mixing to suppress deep convection in a drier environment. This is supported by Derbyshire et al. (2004) showing that the convective cloud top height is very sensitive to the environmental RH. For the shallow plume, ε_0 is directly set to be 3 km^{-1}, same as DP-Z.

Similar to UW, we assume that the fraction of environmental air in the mixture obeys a uniform distribution, then ε_m and δ_m can be calculated as

$$\varepsilon_m = \varepsilon_0 X_c^2,$$

$$\delta_m = \varepsilon_0 (1 - X_c)^2, \tag{11}$$

where X_c is the critical fraction of environment air in the mixture to give a zero buoyancy.

Note that DP-Z and UW only consider the turbulent detrainment and constrained detrainment. However, detrainment of plume air into the environment is assumed to take place by three ways: a turbulent mixing at the lateral boundary of the plume similar to entrainment (δ_m), a forced detrainment (δ_f), and a constrained detrainment (δ_s). Therefore, fractional detrainment rate can be expressed as $\delta = \delta_m + \delta_f + \delta_s$. Within continuously entraining updrafts, in-plume properties tend to be nonuniformly distributed. The properties at the edges of the plume are more environment like, while the core of the plume tends to be undiluted. To consider the impact of such an anisotropy on detrainment, we introduce a forced detrainment. Following Derbyshire et al. (2011), forced detrainment occurs at the level where the buoyancy of the plume starts to decrease with height. It can be formulated as

$$\delta_f = R \frac{1}{\theta_v'} \frac{\partial \theta_v'}{\partial z}, \tag{12}$$

where θ_v' is the virtual potential temperature difference between the plume and the environment ($\theta_v' = \theta_{vu} - \overline{\theta_v}$); R is a tunable parameter, bounded from 0 to 1. Here, we set it to be 0.5, consistent with Derbyshire et al. (2011).

Constrained detrainment only occurs at the top of a plume, where vertical velocity equals to zero. At this level, all the mass in the plume will be detrained into the environment. Thus, the fractional detrainment rate δ_s equals the inverse of the height difference between the plume top and the level below.

d. Convective closure

Convective available potential energy (CAPE) closure has been widely used. Following DP-Z, we treat the closure for deep and shallow plume separately. The closure for the shallow plume is CIN-TKE, same as that in DP-Z. For the deep plume, we assume that the PCAPE generated by the large-scale and PBL processes will be balanced by the deep convection within each time step, namely $(\partial \mathrm{PCAPE}/\partial t)\big|_L = (\partial \mathrm{PCAPE}/\partial t)\big|_{\mathrm{cu}}$. This is called DPCAPE closure as summarized in Table 1.

The PCAPE consumed by convection can be expressed as

$$\left.\frac{\partial \mathrm{PCAPE}}{\partial t}\right|_{\mathrm{cu}} = \int_{z_b}^{z_t} \rho \frac{g}{\overline{T_v}} \left(\frac{\partial \overline{T_v}}{\partial t}\right)\Bigg|_{\mathrm{cu}} dz \approx \int_{z_b}^{z_t} M \frac{g}{\overline{T_v}} \left(\frac{\partial \overline{T_v}}{\partial z} + \frac{g}{C_p}\right) dz,$$

where C_p is the specific heat capacity at constant pressure of dry air and $\overline{T_v}$ is the virtual temperature of the environment; M is the convective mass flux.

Then, the cloud base mass flux M_b can be obtained as

$$M_b = M_b^* \frac{\left.\dfrac{\partial \mathrm{PCAPE}}{\partial t}\right|_L}{\displaystyle\int_{z_b}^{z_t} \frac{g}{\overline{T_v}} \left(\frac{\partial \overline{T_v}}{\partial z} + \frac{g}{c_p}\right) M^* dz}, \tag{13}$$

where M_b^* is the prescribed cloud base mass flux, which can be formulated as $M_b^* = 0.1[\Delta p_{\mathrm{lcl}}/(g\Delta t)]$; Δp_{lcl} is the pressure height of the model layer at the lifting condensation level and Δt is the model integration time step. Note that M^* is the mass flux profile when we use M_b^* as the cloud base mass flux.

e. Cumulus microphysics

Microphysical processes in convection schemes are generally simplified to some key processes. For example, they include an autoconversion process that transforms cloud water/ice to convective precipitation and a rain re-evaporation process that evaporates rain drops in the dry environment. In DP-Z, convective precipitation is a function of liquid/ice water content in the plume and vertical layer depth, as shown in Table 1. However, convective precipitation calculation in DP-THU is treated rather straightforwardly as in UW, following the idea of the Kessler scheme (Kessler 1969). If the condensate q_c in the plume, either cloud ice or cloud water content, is larger than a critical value q_{cr}, the excess condensate will be categorized as precipitation (snow or rain). However, q_{cr} is different between deep and shallow plumes, as the deep plume has a stronger vertical velocity and can maintain more condensates than the shallow plume. The value of q_{cr} is chosen to be 1.0 and 0.5 g kg^{-1} for the deep and shallow plume, respectively. Snow falling below the melting level will be melted to rain instantaneously.

Rain re-evaporation in DP-THU uses a different parameterization from DP-Z. Following Sundqvist (1988), this process can be formulated in the form of

$$E = k(1 - \mathrm{RH})\sqrt{P}, \tag{14}$$

where P is the precipitation flux (kg m^{-2} s^{-1}), RH is relative humidity of the environment, and E is the evaporation rate (kg kg^{-1} s^{-1}); k is a tunable parameter to control evaporation strength and is set to be 0.5×10^{-5} kg$^{-1/2}$ m s$^{-1/2}$.

f. Coordination with other schemes

The variables needed by DP-THU are not only from the host model, such as pressure, temperature, and specific humidity, but also from the PBL scheme, including TKE and planetary boundary layer height (PBLH). In addition, the cloud macrophysics scheme needs the outputs from the DP-THU scheme, including convective cloud fraction and detrainment rate. Here, we introduce our strategies to coordinate with these schemes.

The PBL scheme used in CAM5 is a moist turbulent scheme with a diagnosed TKE, developed by Grenier and Bretherton (2001) and applied to CAM5 by Bretherton and Park (2009) with some modifications. TKE is diagnosed by neglecting its storage term and PBLH is diagnosed by the Richardson number in the scheme. The scheme categorizes the PBL into stable, stable-turbulence, and convective layers with regime-dependent procedures. Therefore, we can directly use the TKE and PBLH from the PBL scheme.

The proportion of ice and supercooled water detrained from the convection scheme has a large impact on the formation of mixed-phase clouds (Zhang et al. 2020). In the DP-THU scheme, detrainment contains water vapor, liquid water, and ice water. However, the macrophysics scheme in CAM5 has its own module to partition detrained convective condensate into liquid and ice based on temperature. To avoid the conflict, we assume that the detrained condensate from DP-THU is liquid water, similar to UW.

A brief summary of the DP-THU scheme and its differences from DP-Z and UW is in Table 1. Similar to UW, DP-THU uses θ_{il} and q_t as the conservation variables, while DP-Z uses q_t and h_{il}. Note that both θ_{il} and h_{il} are not exact conservative variables. As evaluated by Bryan and Fritsch (2004), conventionally defined θ_{il} will have a positive bias over 5 K in the upper troposphere during an adiabatic ascent due to large condensate loadings. In fact, h_{il} is more accurate compared to θ_{il}, but could be still nonconservative because convective plumes are far from a hydrostatic system (Romps 2015). With the condensate loading capped at 1 (0.5) g kg^{-1} in the deep (shallow) plume, the inaccuracy of θ_{il} can be largely minimized. We will compare the impact of using θ_{il} and h_{il} on the overall model performance in a future work. The trigger and closure of shallow convection is identical to the DP-Z and UW, but a modified DPCAPE-type trigger and closure is adopted for the deep convection in DP-THU. Fractional mixing rates are different for the deep and shallow plume following DP-Z. For the shallow plume, a constant mixing rate of 3 km^{-1} is chosen as in DP-Z, while a relative humidity dependent mixing rate is applied for the deep plume to inhibit deep convection in a hostile environment with a different form from DP-Z (Table 1). Similar to UW, only autoconversion of cloud condensates, melting or freezing, and re-evaporation of rain and snow are included in DP-THU. A Kessler-type autoconversion parameterization is adopted with a different threshold for deep and shallow plume (Table 1). Rain re-evaporation followed the Sundqvist (1988) method.

3. Single-column model test

A single-column model (SCM), with prescribed large-scale forcing, is an efficient way to test and evaluate new physical parameterizations (Gettelman and Morrison 2015; Randall et al. 1996). We choose the Tropical Warm Pool–International Cloud Experiment (TWP-ICE; May et al. 2008) as a typical case to test the new scheme. There are three distinctive periods in TWP-ICE. The active monsoon period started at 19 January 2006, culminating with a large mesoscale convective system (MCS) that passed through the observational domain on 23–24 January and ended at 26 January. Then, a suppressed monsoon period followed, accompanied by the development of shallow convections. Until 3 February, it became a monsoon break period (May et al. 2008).

A series of single-column simulations were conducted from 18 January to 3 February, including a default run (DEF-SC, with ZM deep convection and UW shallow convection), a control run (CTL-SC, with the new double-plume convection scheme), and some sensitivity tests with different rkm [see Eq. (10) for the introduction of the term rkm]. A series of sensitivity tests for the fractional mixing rate (ε_0) of the deep plume are conducted. The term ε_0 is an important parameter for the deep plume as it impacts the turbulent entrainment rate, mass flux profile, and in-plume properties. We modify ε_0 by changing the rkm value from 1.0 km^{-1} to 0.3, 0.5, 0.8, 1.2, and 1.4 km^{-1}. Simulations use 30 vertical layers with a time step of 20 min, driven by the same large-scale forcing data from Xie et al. (2010). We examine convection related variables, including cloud fraction, precipitation, convective mass flux profile, and in-cloud buoyancy.

The precipitation rates are similar among all simulations and consistent with the observation (Fig. 1), as precipitation in SCM simulations is basically constrained by the large-scale forcing. Heavy rainfall occurs during the active monsoon period with a peak of ~7.8 mm h^{-1} and weak rainfall ($<$1.5 mm h^{-1}) appears during the monsoon suppressed period. Compared to DEF-SC, CTL-SC tends to have a slightly larger precipitation rate during the active monsoon period, which is closer to the observation.

The vertical profiles of cloud fraction during the two periods are illustrated in Fig. 2. During the active monsoon period (Fig. 2a), although all these simulations severely overestimate the cloud fraction above 700 hPa (i.e., midcloud and high cloud) by a factor of 1.5, they can successfully capture the peak near 250 hPa. DEF-SC slightly overestimates the low clouds by 10%, while CTL-SC agrees better with the observation, which is mainly caused by the different treatment of

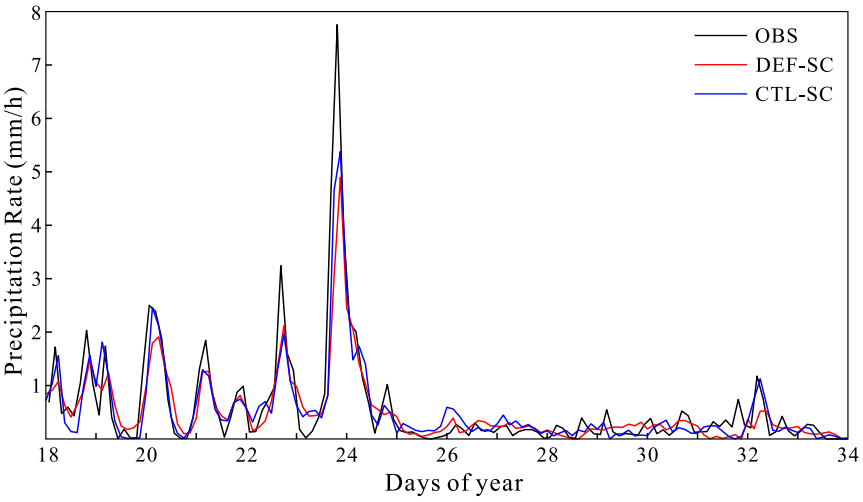

FIG. 1. The time series of precipitation rate from SCM. The frequency of observation and model output is 3 h.

convective cloud amount in the two schemes. In DP-THU, convective cloud fraction is directly calculated from the updraft mass flux and vertical velocity of the plume, while it is solely diagnosed from the convective mass flux in ZM. In general, the diagnosed convective cloud amount is much larger than that directly calculated.

During the suppressed period (Fig. 2b), DEF-SC has more low and midcloud amounts, but much less high cloud compared to observations. Instead, CTL-SC captured cloud fraction much better with comparable high cloud amounts with observed near 200 hPa. This is because the relative humidity in the upper troposphere is higher during the suppressed period in CTL-SC than DEF-SC, resulting from the larger detrainment during the active monsoon period as manifested by the top-heavy mass flux profile in CTL-SC (Fig. 4). In addition, the low and midcloud amounts are better captured by CTL-SC although the altitude of peak is slightly too high at 700 hPa instead of 900 hPa in observations. This

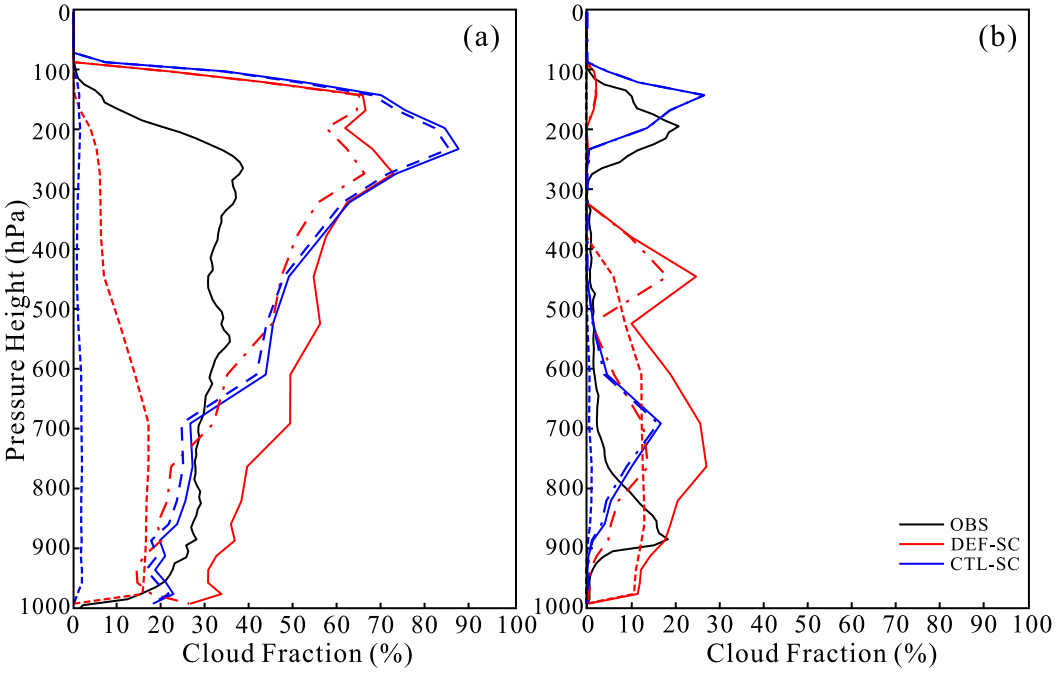

FIG. 2. Vertical profiles of cloud amounts, showing the time-averaged profile during (a) the active monsoon period and (b) the monsoon suppressed period. The dashed lines represent the clouds from convection scheme while the dash-dotted line represents the clouds from macrophysics scheme.

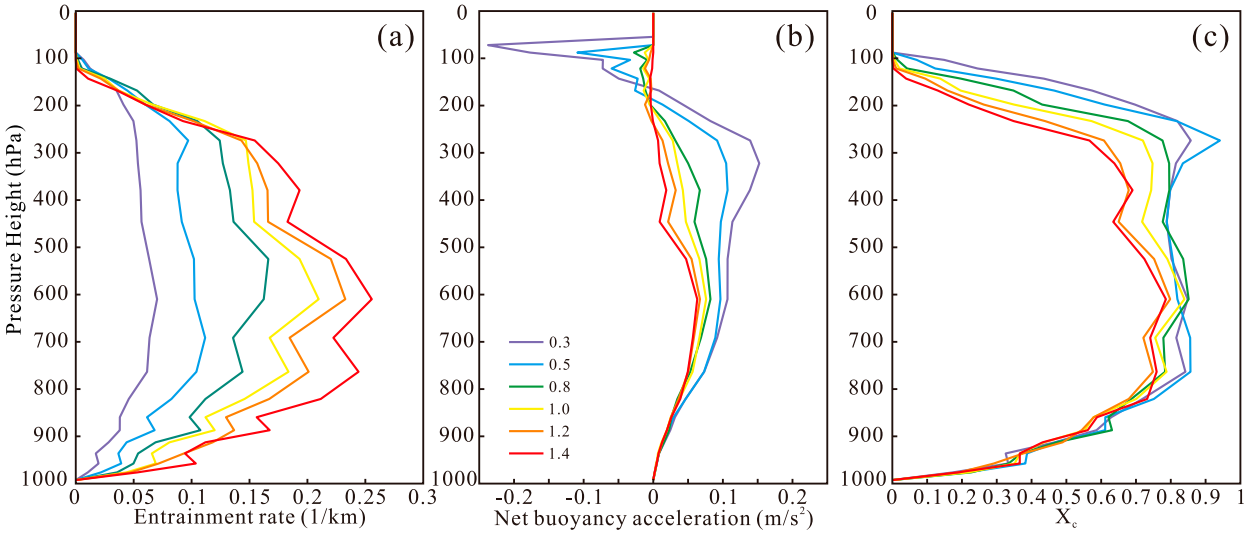

FIG. 3. Vertical profile of (a) entrainment rate, (b) net buoyancy acceleration, and (c) critical mixing fraction. The colors of the lines indicate different rkm simulations (km^{-1}) shown in (b).

suggests that the double-plume scheme is able to mitigate the too frequent occurrence of deep convection noted in ZM.

For sensitivity tests, we mainly focus on the simulation results during the active monsoon period dominated by deep convection. As shown in Fig. 3a, ε_0 is larger in the midtroposphere, but becomes smaller in the lower and upper troposphere due to the vertical distribution of relative humidity. Larger ε_0 will lead to a larger ε, and thus more dilution of the plume. However, the dependence of ε on ε_0 is not linear due to the contribution of X_c. A plume with more ambient air entrained has a smaller buoyancy (Fig. 3b) and thus smaller X_c (Fig. 3c), as X_c is proportional to plume buoyancy in the buoyancy sorting method.

During the active monsoon period, the double-plume scheme produces a top-heavy mass flux profile. This is different from DEF-SC (Fig. 4a), which has a peak near 700 hPa. Top-heavy mass flux profiles imply a large detrainment at the top of the plume and thus help the formation and maintenance of high clouds (Fig. 2). Differently, DEF-SC has a larger detrainment in the midtroposphere between 600 and 400 hPa, and thus leads to a positive cloud amount bias at these levels (Fig. 2).

Sensitivity tests do not show obvious differences for the mass flux profile with various ε_0 (Fig. 4a). This is probably related to the DPCAPE closure used, in which convection with larger mass flux can consume more PCAPE and thus

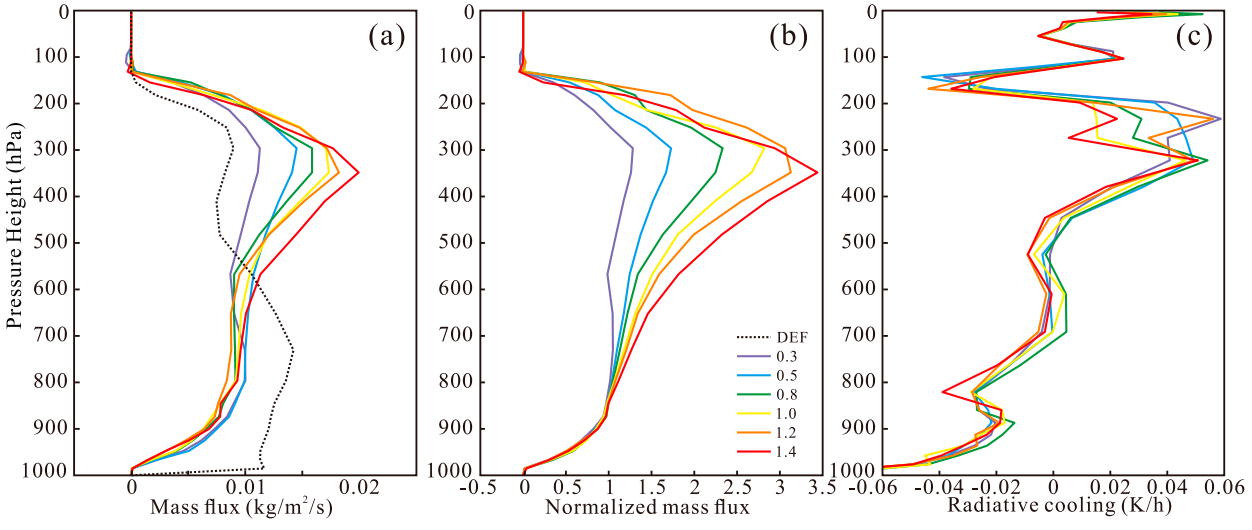

FIG. 4. Vertical profile of (a) mass flux of deep convection, (b) normalized deep convection mass flux by cloud base mass flux for various simulations, and (c) radiative cooling. The profile is drawn from the time average of deep plume mass flux output at each time step during the active monsoon period. The colors of lines indicate different rkm simulations shown in (b).

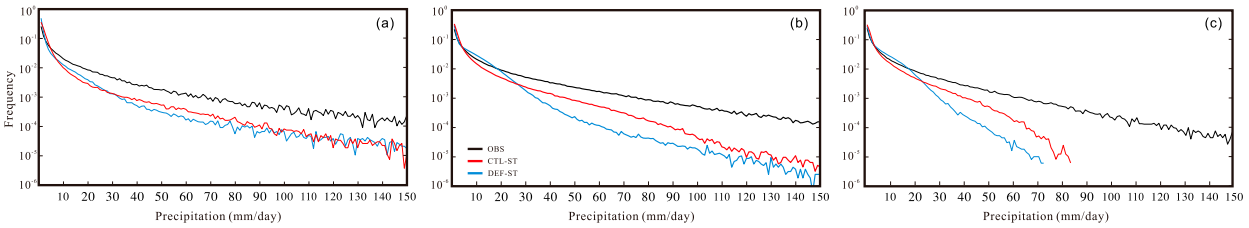

FIG. 5. Precipitation strength distributions, showing the results from the (a) f05, (b) f09, and (c) f19 simulations.

tends to have a smaller cloud base mass flux. Therefore, the time-averaged mass flux profiles are similar. However, when normalized by their cloud base mass fluxes (Fig. 4b), the differences among simulations become more distinctive. The plume with larger ε_0 tends to entrain more and thus has a more top-heavy, but slightly lower-peaked mass flux profile in convection favorable environment (Fig. 4b), consistent with the above reasoning.

4. Short-term hindcast simulations

Short-term hindcast simulation is an effective way to evaluate model performance directly related to fast physical processes (Ma et al. 2014; Xie et al. 2012). We focused on the impacts of the scheme on tropical precipitation diurnal cycle and strength at different spatial resolutions. We conducted three sets of daily hindcast simulations with different spatial resolutions of f05 (~50 km), f09 (~100 km), and f19 (~200 km) based on the Cloud Associated Parameterization Testbed (CAPT) dataset (Hannay et al. 2009; Phillips et al. 2004). Each daily hindcast is integrated for 5 days from 1 October through 28 October 2008, initialized using the data provided by Ma et al. (2015) and Zheng et al. (2016). Similar to previous studies, we use the third-day forecast for comparisons with observations. The short-term hindcast simulations with ZM are labeled DEF-ST while the simulations with DP-THU are labeled CTL-ST. We mainly evaluated the tropical precipitation variations using the Tropical Rainfall Measuring Mission (TRMM) dataset (Acker and Leptoukh 2007).

a. *Precipitation intensity*

Tropical 3-hourly TRMM precipitation data were interpolated to simulation resolutions by an area conservative remapping method for precipitation intensity comparison (Fig. 5). As noted in previous studies (Wang and Zhang 2016), tropical precipitation frequency decreases very quickly with intensity using ZM, especially for low-resolution simulations (Figs. 5b,c), resulting in the so-called "too frequent light rain" phenomenon in GCMs (Pendergrass and Hartmann 2014; Wang and Zhang 2013). This is much improved using DP-THU, although the scheme still underestimates the frequency of intense precipitation. With increased resolution, the difference between the two schemes becomes smaller due to increased large-scale precipitations (not shown). In addition, the zero-precipitation frequency in CTL-ST is larger than DEF-ST.

b. *Precipitation diurnal cycle*

Precipitation diurnal cycle over tropical lands is also a big challenge for cumulus parameterizations (Cui et al. 2021). We selected three typical regions having dominant diurnal cycle signals, including the Maritime Continent, the Amazon, and tropical Africa (blue boxes in Fig. 13b), for evaluation. Observed precipitation has its minimum at 0900 LST and peaks in the late afternoon (1500 or 1800 LST) with a magnitude ~3 times of the minimum over the three regions. In contrast, DEF has a much weaker diurnal variation, especially over the Maritime Continent (Fig. 6a). CTL is able to better capture the strength of diurnal variation with a delayed afternoon peak compared to DEF over Amazon, but its peak time

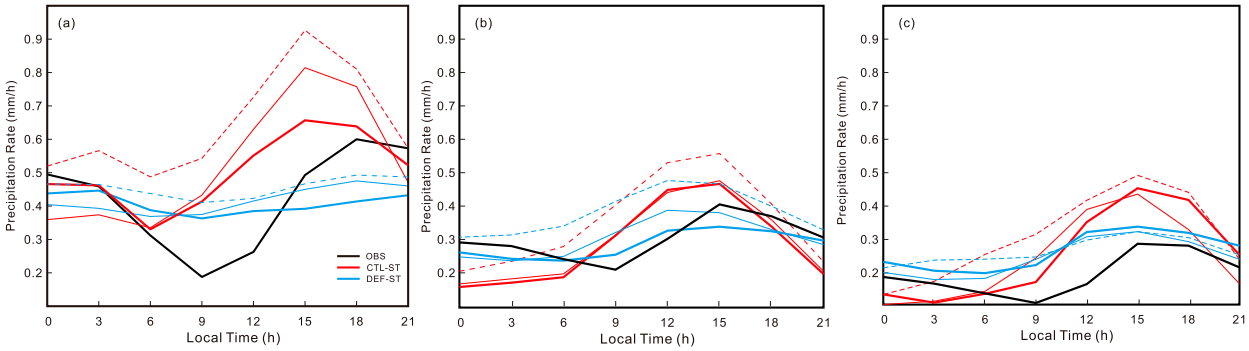

FIG. 6. The precipitation diurnal cycle of (a) the Maritime Continent, (b) the Amazon, and (c) tropical Africa. Dashed, thin solid, and thick solid lines represent the results from the f05, f09, and f19 simulations respectively.

TABLE 2. Global mean climatological properties of DEF, CTL, and observations. The number in square brackets represents the root-mean-square error (RMSE) of the variables. The source of observations can be found in the text. Cloud amounts are diagnosed using the COSP simulator for a better comparison with observations.

	DEF	CTL	OBS
Precipitation rate (mm day^{-1})	3.02 [1.16]	2.92 [1.30]	2.674
Low cloud amount (*CALIPSO*; %)	31.98 [11.31]	33.28 [10.24]	38.37
High cloud amount (*CALIPSO*; %)	26.24 [8.16]	30.24 [6.79]	32.04
Total cloud amount (*CALIPSO*; %)	55.00 [15.06]	58.33 [12.69]	67.25
Shortwave cloud forcing (W m^{-2})	−49.31 [13.58]	−44.72 [10.70]	−47.15
Longwave cloud forcing (W m^{-2})	22.52 [6.52]	24.31 [8.33]	26.06
Net TOA radiation (W m^{-2})	4.09 [10.96]	7.61 [11.77]	0.81
Net TOA longwave radiation (W m^{-2})	237.65 [6.50]	236.56 [9.12]	239.67
Net TOA shortwave radiation (W m^{-2})	241.74 [12.17]	244.17 [12.07]	240.48

is still 3 h too early over the Maritime Continent. Tropical rainfall is dominated by mesoscale convective system in general. However, most convective schemes have not considered convective organizations and thus might have a problem with diurnal variations.

5. AMIP simulations

a. General performance

The simulations use a finite-volume dynamic core (Neale et al. 2012) with a horizontal resolution of 0.9° × 1.25° and 30 layers in the vertical. The model is run for 6 years with prescribed monthly mean sea surface temperature and sea ice from the Hadley Centre (Rayner et al. 2003). We averaged the last 5 years of the simulations to compare with the observed climatologies with the first year discarded as the spinup. The settings of default simulation (DEF) and control simulation (CTL) are the same except that the ZM deep convection is turned off while UW is replaced by DP-THU in the control simulation. In addition, the Coupled Model Intercomparison Project Observation Satellite Package (COSP; Kay et al. 2012; Bodas-Salcedo et al. 2011) is turned on for a better comparison between simulated and observed clouds.

We focused on those variables related to convection, including precipitation, clouds, and radiation. Precipitation from Global Precipitation Climatology Project (GPCP; Huffman et al. 2009) and the longwave and shortwave radiation from Cloud and the Earth's Radiant Energy System Energy Balanced and Filled (CERES-EBAF; Loeb et al. 2009) were used. Note that the global mean precipitation simulated by most GCMs is greater than GPCP observation by about 10%–15% (Zhao et al. 2018a), as the GPCP dataset might bias low (Gehne et al. 2016). In addition, the longwave cloud forcing (LWCF) and shortwave cloud forcing (SWCF) data from CERES-EBAF also contain an uncertainty of about 15% (Loeb et al. 2009). Cloud amount from the GCM-oriented *CALIPSO* cloud product (Chepfer et al. 2010) is chosen for comparison.

Mean climate statistics from the default simulation (DEF), control simulation (CTL), and observations are summarized in Table 2. The global average precipitation rate decreased from 3.02 mm day^{-1} in DEF to 2.92 mm day^{-1} in CTL, closer to the observation (Table 2), but the RMSE is slightly increased in CTL. Wet bias is distributed from the southern Indian Ocean, through Somalia to the north Indian Ocean, as well as tropical Pacific and southern foothills of the Himalayas with dry biases over the equatorial eastern Indian Ocean and Amazon area in DEF (Fig. 7d). These biases are partly alleviated in CTL (Fig. 7e), especially over the Indian Ocean and southern Amazon (Fig. 7f). However, some biases are exaggerated, such as those over the southern foothills of the Himalayas and the Maritime Continent (Fig. 7f). Overall, the new scheme tends to produce more precipitation over the tropical land areas, but less precipitation over the tropical oceans than DEF (Fig. 7f). Such changes are dominated by convective precipitation, which is over 90% of the total precipitation over the tropics (Fig. 7h). Convective precipitation decreases over the tropical Indian Ocean, the tropical Pacific Ocean, the Arabian Sea, and the Bay of Bengal, as well as the northern Amazon and storm track of South Pacific, and increases over the Maritime Continent, the western tropical Pacific, and the foothills of the Himalayas and Rocky Mountains (Fig. 7i). The strong increase of convective precipitation in the mountainous area is due to the use of CIN-TKE triggers, as the TKE in these areas is large, leading to more triggered convection and convective precipitation. Large-scale precipitation change is small with increases over the tropical Africa and South America (not shown).

Compared with DEF, clouds in CTL are significantly improved. Both high and low cloud amounts are closer to the observation with a reduced RMSE (Table 2). Observation shows that low clouds tend to appear in the eastern subtropical oceans due to large-scale subsidence and relatively low sea surface temperature there. Typically, there exists a strong boundary layer inversion (large CIN), with moderate TKE within the boundary layer. Therefore, moist convection is inhibited. As the water vapor cannot effectively be pumped up into the upper troposphere, a cloud-capped boundary layer forms with large low cloud coverage in these regions. The simulation with the original scheme performs poorly in capturing this pattern as convection is frequently triggered in these regions. Therefore, DEF severely underestimates the low cloud amounts over the subtropical ocean by over 40%

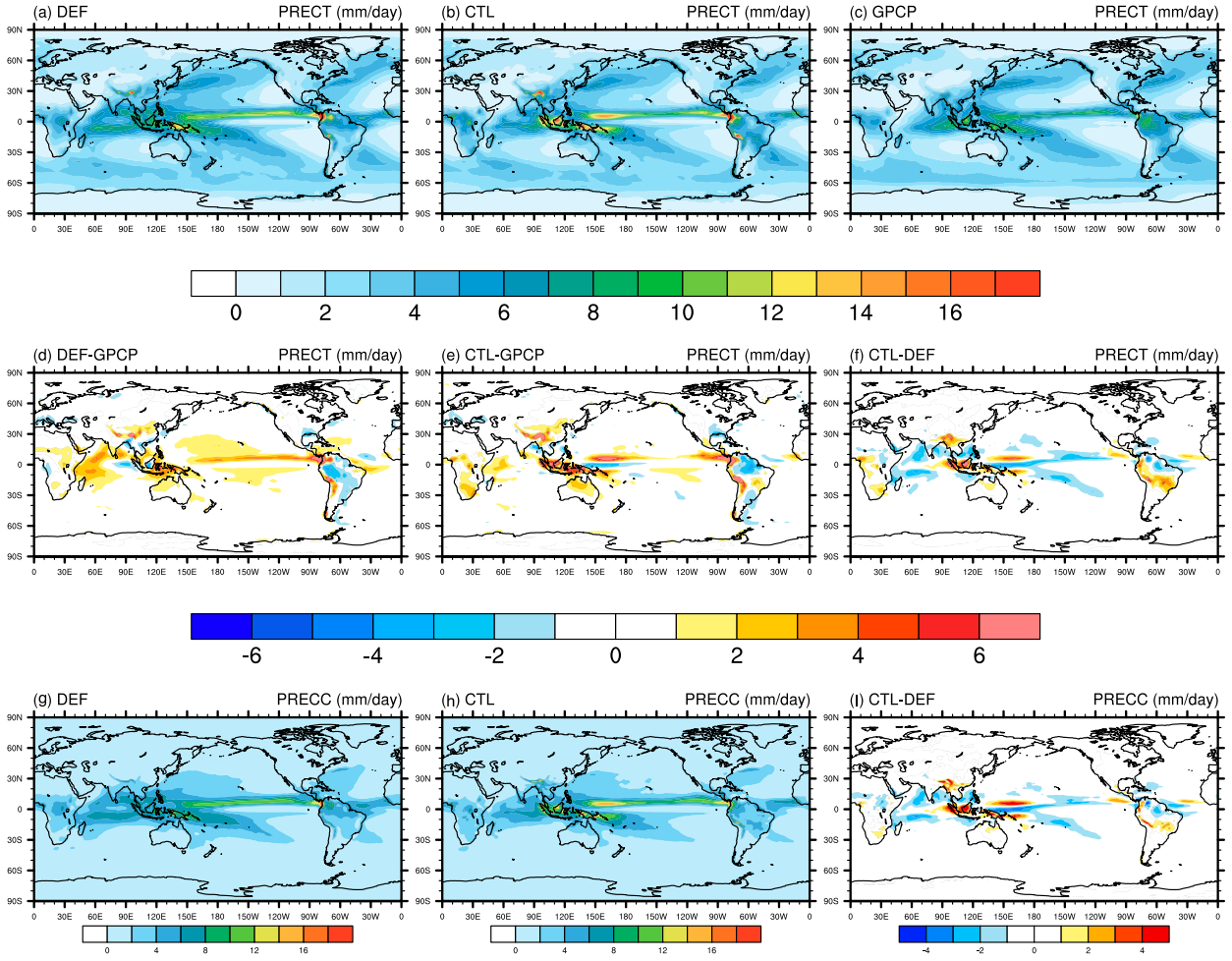

FIG. 7. Annual mean precipitation from (a) DEF, (b) CTL, and (c) GPCP, and the differences between (d) DEF and GPCP, (e) CTL and GPCP, and (f) CTL and DEF. Also shown is the convective precipitation from (g) DEF and (h) CTL, as well as (l) their difference.

compared to the observation. The new scheme largely alleviated this bias, partly because the CIN closure is also used for deep convection in the new double-plume convective parameterization, reducing the triggering of convection. As a result, the prominent negative bias of low cloud amounts in the subtropical ocean has been reduced (Fig. 8e). Note that low clouds are reduced over land in CTL compared to DEF (Fig. 8f). This is because low clouds over tropical lands are dominated by lower-troposphere convective clouds rather than stratocumulus, which is different from the situation of eastern subtropical oceans. In DEF, due to the CAPE trigger (CAPE $>$ 70 J kg^{-1}) in ZM, convection that cannot penetrate to their levels of free convection (LFCs) is also triggered. This is probably part of the reason for the too frequent short-duration deep convection and convective clouds using ZM. However, such types of deep convections are suppressed in DP-THU because of the use of the CIN-TKE based trigger, as the tropical lands have large CIN (e.g., Riemann-Campe et al. 2009), leading to less convective clouds in the model. In addition, as mentioned in section 3, cloud fraction is directly calculated from the vertical velocity of the plume in DP-THU, while it is diagnosed from the convective mass flux in ZM. The method in DP-THU tends to produce smaller cloud faction than that in ZM in general as in SCM simulations.

High clouds appear over the deep tropics (western Pacific, Maritime Continent, tropical Africa, and ITCZ) where abundant cloud condensates were pumped into the upper troposphere to form high clouds by deep convection. Compared to DEF, the new scheme tends to produce more high clouds over the deep tropics (Fig. 9f), which help alleviate the negative bias in DEF (Fig. 9d). The new scheme tends to develop stronger and deeper convection over these regions and transport more water vapor and condensate to the upper troposphere because of a top-heavy mass flux profile as noted above (cf. Fig. 4a).

Cloud regime transition is also evaluated along a typical cross section offshore California from 35°N, 125°W to 1°S, 173°W, proposed by Global Energy and Water Cycle Experiment (GEWEX) Cloud System Studies (GCSS) Pacific Cross-section Intercomparison (GPCI; Yu et al. 2017). Along this

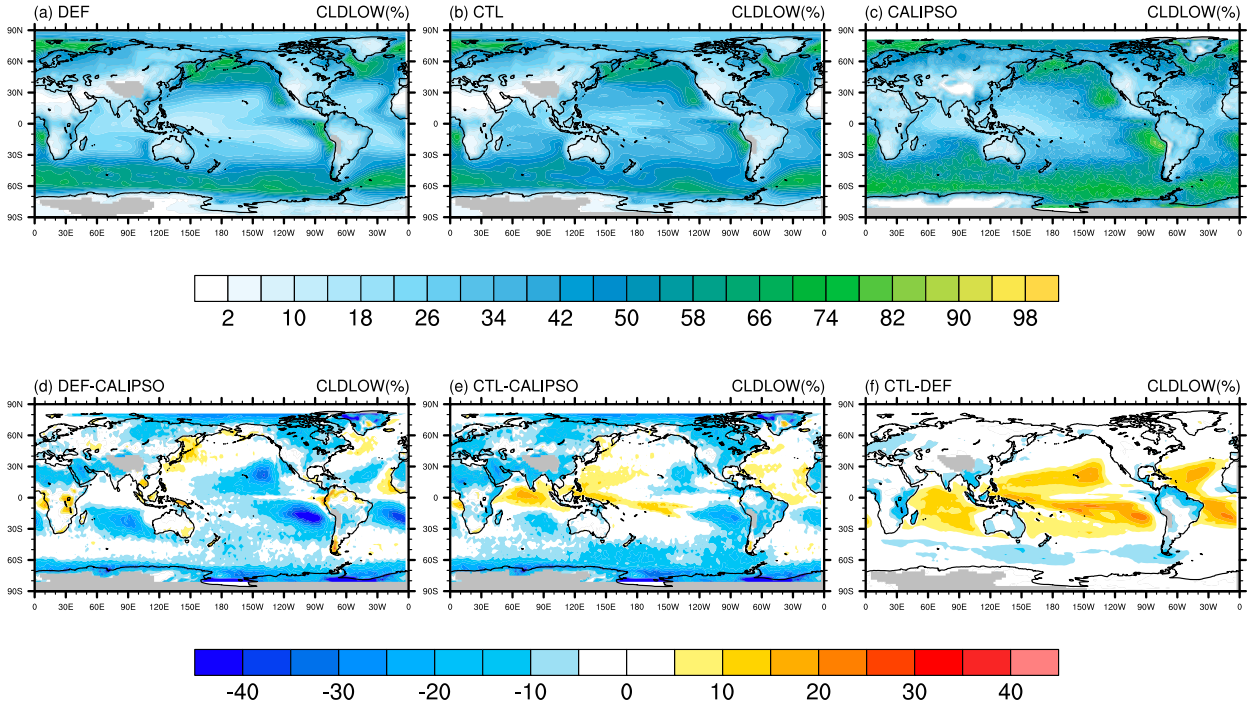

FIG. 8. As in Fig. 7, but for annual mean low cloud fraction (%). The observation data are from the GCM-oriented *CALIPSO* cloud product.

cross section (Fig. 10), cloud type transits from boundary layer stratus via stratocumulus to shallow cumulus and then deep cumulonimbus. In the observation (Fig. 10), total cloud amounts have two peaks, with one located at the shallow cumulus regime near 135°W and another located at the deep cumulonimbus regime around 165°W. Both DEF and CTL can capture this cloud regime transition. However, low cloud amounts decrease sharply west of 130°W in DEF, while the

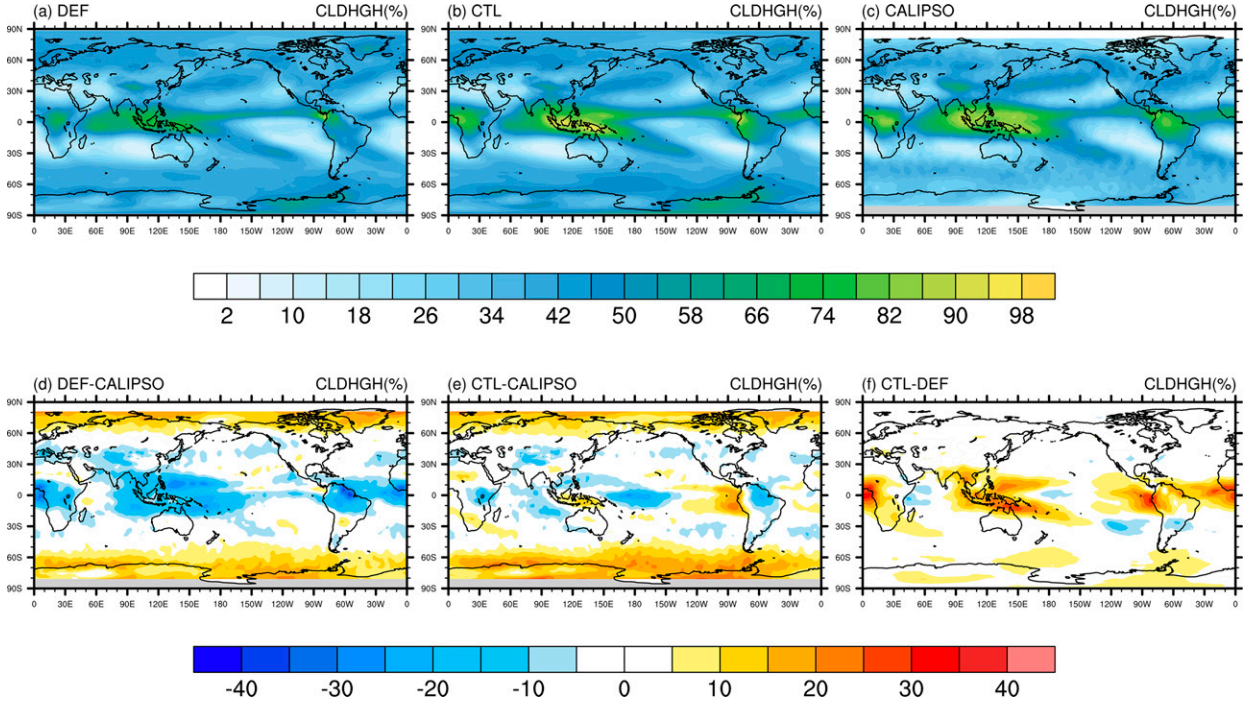

FIG. 9. As in Fig. 7, but for annual mean high cloud fraction (%).

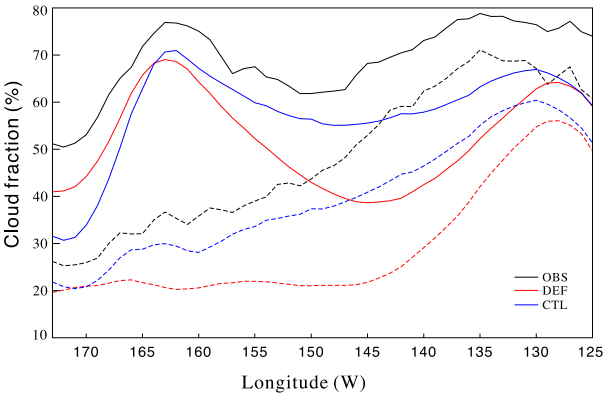

FIG. 10. The cross section of cloud regime transition offshore the California as in GPCI experiment. The solid lines represent the total cloud amounts while the dashed lines indicate the low cloud amounts.

decrease is more gradual in CTL. Compared to DEF, CTL produced more low clouds within the shallow cumulus regime, closer to observations. In the deep convection regime, both CTL and DEF perform well in capturing the peak near 165°W.

In addition to cloud amounts, cloud radiative forcing is also closely regulated by cloud optical depths, which are related to cloud water path. With the change of cloud fraction and liquid water path (LWP), cloud radiative forcing also changes correspondingly using the new scheme. The global mean SWCF decreases from -49.31 W m^{-2} in DEF to -44.44 W m^{-2} in CTL (Table 2), with a reduced RMSE from 13.58 to 10.93 W m^{-2}. For the spatial distribution, the largest difference between CTL and DEF is the increased SWCF at ITCZ regions and tropical continents (Fig. 11f). SWCF increases at ITCZ regions due to the decrease of LWP but increases at tropical continents because of reduced low cloud amount (Fig. 11f) and LWP (not shown) there. With increased low clouds over the subtropical ocean, positive SWCF biases are alleviated there (Fig. 11e).

SWCF is mainly affected by the cloud optical depth, but LWCF is dominated by cloud top temperature. Compared to DEF (22.52 W m^{-2}), the global mean LWCF increased to 24.31 W m^{-2} in CTL, closer to the observation of 26.06 W m^{-2} (Table 2). The most notable change of LWCF between CTL and DEF corresponds well with the precipitation change (Fig. 8f) and is confined to the tropics (Fig. 12).

b. *Sensitivity tests*

Some key parameters in the convection scheme are hard to be observationally or theoretically constrained, but have significant impacts on GCM simulations (e.g., Yang et al. 2013; Lin et al. 2013; Zhao et al. 2018b; Lin 2019). A series of sensitivity tests via modifying fractional mixing rate ε_0 and rain evaporation rate k of the deep plume are conducted. These two parameters were found to have great impacts on global simulations (Zhao et al. 2018b). Similar to the SCM, rkm is altered from the value of 1 km^{-1} in the CTL to other values (Table 3). Note that a decrease of rkm means reduced mixing

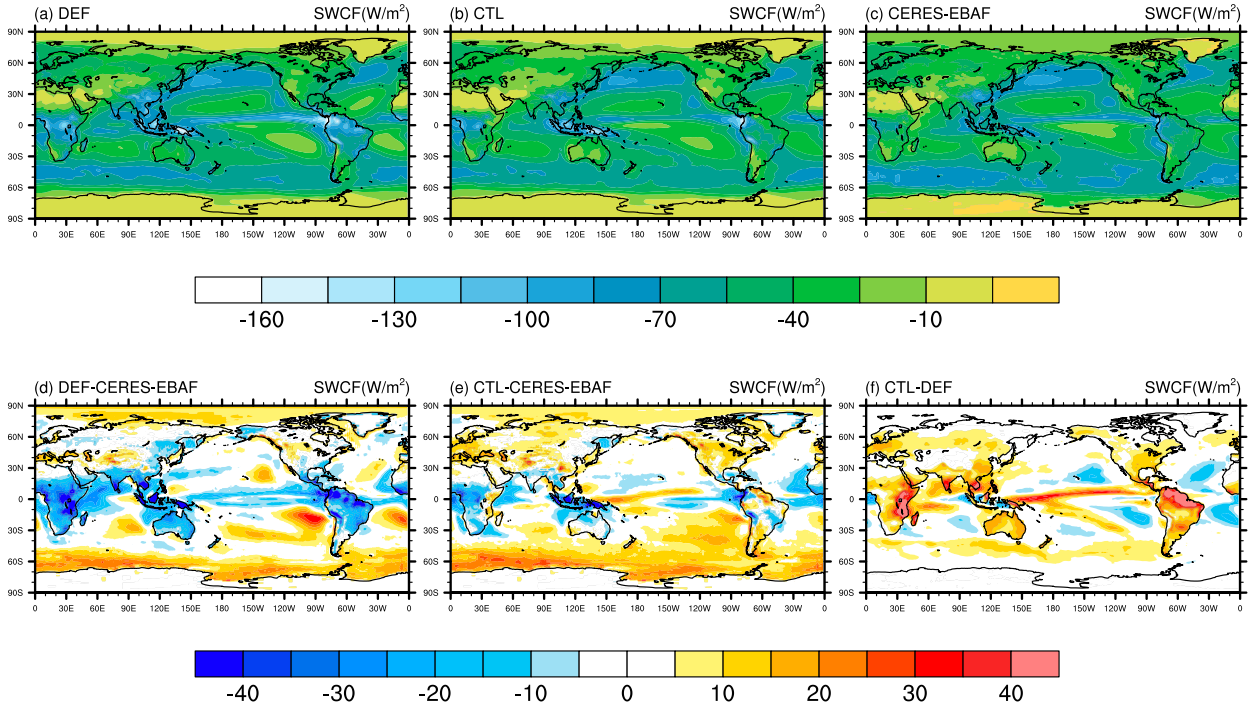

FIG. 11. As in Fig. 7, but for annual mean shortwave cloud forcing (W m^{-2}). Observation data are obtained from Cloud and the Earth's Radiant Energy System Energy Balanced and Filled (CERES-EBAF).

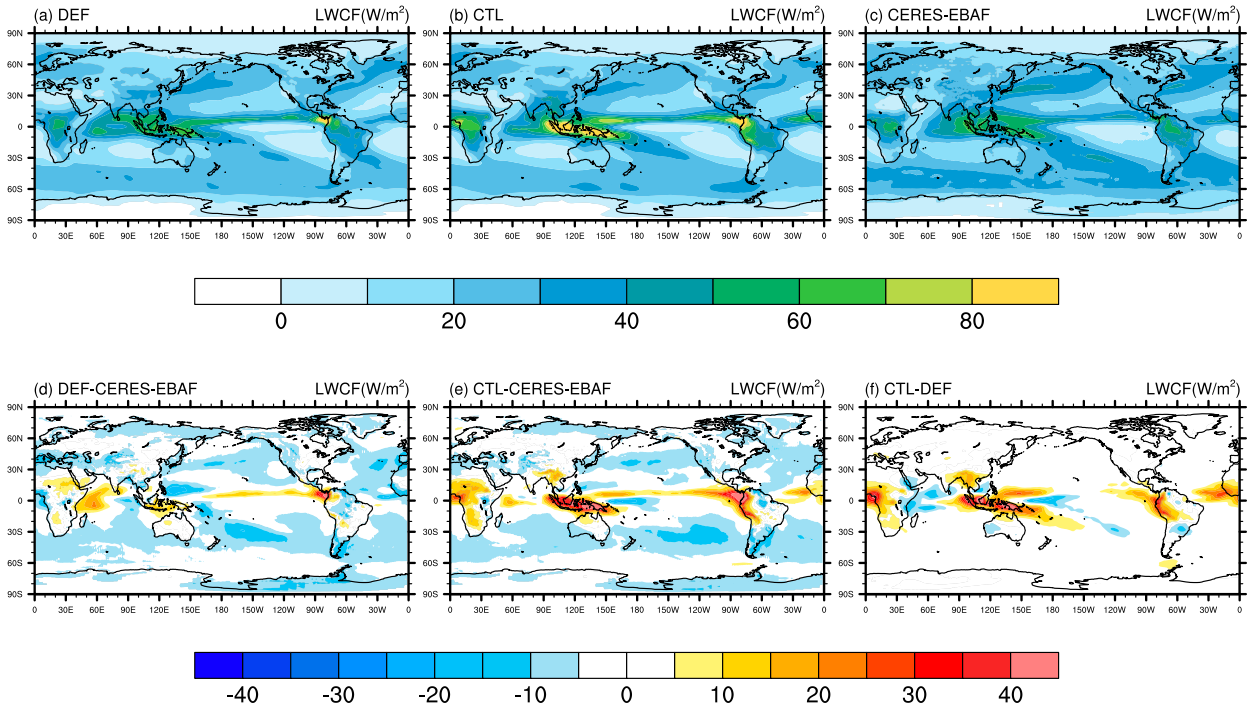

FIG. 12. As in Fig. 7, but for longwave cloud forcing (W m^{-2}).

of updrafts with environment and an enhancement of deep convection. Oppositely, a larger rkm indicates a more efficient mixing between the plume and environment and generally produces a less penetrative plume. Therefore, the convection tends to be suppressed. In addition, changing the strength of convection will alter the top of the atmosphere (TOA) radiation balance, as the vertical distribution of clouds and condensates will be changed too. Another group of simulations varying the rain evaporation rate was also conducted (Table 3), as some studies indicated that rain re-evaporation may have a direct impact on tropical precipitation (Bacmeister et al. 2006) and an indirect effect on cloud radiative forcing (Sui et al. 2020) via changing the precipitation efficiency.

Although the convective precipitation monotonically increases with decreased rkm, as the convections become stronger when mixing rate of the plume is reduced, global mean precipitation decreases slightly with decreased rkm (Table 3). However, the spatial distribution of tropical precipitation changed significantly with rkm (Fig. 13), especially over the warm pool and Amazon region. Precipitation increases in the tropical western Pacific, the Philippine Sea, and the Amazon, but decreases over the Indian Ocean and the Maritime Continent region with increased rkm (Fig. 13a). In contrast, with decreased rkm, precipitation increases over the tropical mideastern Pacific and equatorial Indian Ocean. Such a dependence of precipitation on mixing rate is similar to that noted in Zhao et al. (2018b).

TABLE 3. A brief summary of sensitivity tests. Note that cloud amounts are from the COSP simulator for a better comparison with observations.

	EXP1	EXP2	EXP3	EXP4	EXP5	EXP6	EXP7	EXP8
rkm	2.0	1.5	0.5	0.2	1.0	1.0	1.0	1.0
k (10^{-5} $kg^{-1/2}$ $m\ s^{-1/2}$)	0.5	0.5	0.5	0.5	0.9	0.7	0.2	0.1
Net TOA radiation (W m^{-2})	6.40	7.26	6.56	4.03	7.38	7.62	7.23	6.88
Net TOA shortwave radiation (W m^{-2})	245.82	245.33	242.25	240.10	243.98	244.04	244.33	244.41
Net TOA longwave radiation (W m^{-2})	239.42	238.07	235.69	236.07	236.60	236.42	237.10	237.53
LWP (g m^{-2})	33.54	33.02	36.78	39.74	35.77	35.02	32.78	32.30
Low cloud amount (*CALIPSO*; %)	32.04	32.37	34.89	36.68	33.29	33.29	33.26	33.20
High cloud amount (*CALIPSO*; %)	27.55	28.99	30.39	29.02	30.00	30.20	30.14	29.91
Precipitation rate (mm day^{-1})	3.00	2.96	2.89	2.89	2.90	2.90	2.96	2.98
Convective precipitation rate (mm day^{-1})	1.75	1.83	1.88	1.91	1.79	1.83	1.97	2.01

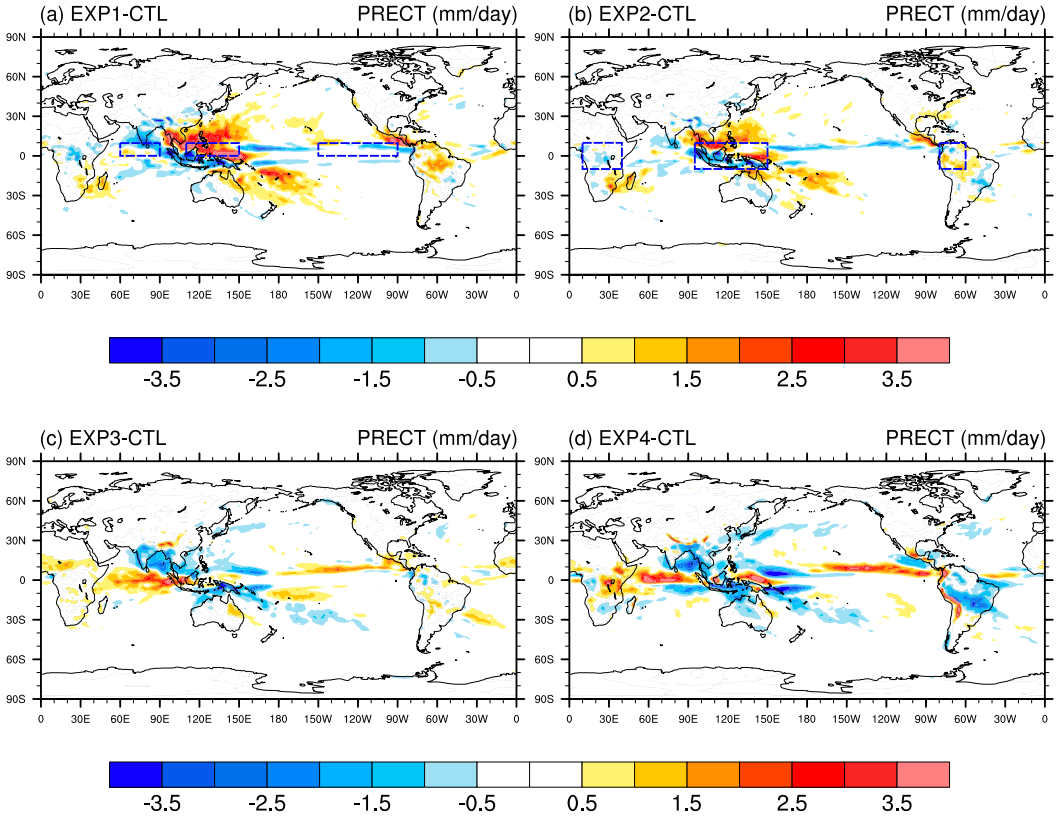

FIG. 13. (a),(b) Annual mean precipitation difference between various fractional mixing rate experiments and CTL. The three blue rectangle boxes in (a) from left to right denote the TIO, WP and EP regions, respectively. The three blue rectangle boxes in (b) from left to right denote the tropical Africa, Maritime Continent, and Amazon regions, respectively.

The most distinctive changes in Fig. 13 are over the tropical eastern Pacific (EP), the western Pacific (WP), and the tropical Indian Ocean (TIO). Therefore, we take these three regions as examples for further investigation. Among these three regions, the most robust change is the monotonically increased upper-troposphere temperature with decreased rkm (Fig. 14). Zhao et al. (2018b) noted that the upper-tropospheric temperature is likely determined by the temperature of the deep convective plumes. Deep plumes with larger rkm, namely more diluted and colder plumes, will lead to a colder upper troposphere (Donner 1986). One thing to note is that increased rkm does not warm the lower troposphere over the EP (Fig. 14c) compared to the WP and TIO (Figs. 14a,b).

However, specific humidity change is more diverse and regime dependent. In the WP region, upper-troposphere (above 550 hPa) moisture varies negligibly compared to the mid- and lower troposphere when we alter the rkm (Fig. 15b). Increasing rkm will significantly moisten the lower troposphere due to increased mixing between the plume and ambient air, leading to more detrainment there. Therefore, the collective impact of an increased rkm is the colder upper troposphere and a wetter lower troposphere, and thus more precipitation due to destabilized atmosphere over WP. Decreasing rkm has the opposite effect. However, in the TIO and EP, the environment is not as friendly as WP for convection. Therefore, decreasing rkm will make the plume more penetrative and higher, increasing not only the upper troposphere temperature but also the specific humidity. Increasing rkm will dilute and suppress the plume, making the upper troposphere colder and drier (Figs. 15a,c).

Cloud amounts and TOA radiation are also influenced by rkm. TOA net shortwave radiation is significantly influenced by the cloud optical depth and cloud amounts. Low cloud amount monotonically increases with decreased rkm, while LWP decreases first in experiment 2 and then increases with decreased rkm. Their collective effect leads to a monotonically decreasing net TOA shortwave radiation with decreased rkm. However, it is more complex for TOA longwave radiation as it is dominated by the high cloud amount and height. Simulation results indicates that high clouds amount is not monotonic to rkm. Although a plume with smaller entrainment rates can penetrate higher, it does not necessarily detrain more water vapor and condensate into the upper troposphere due to its small mass flux at the top of the plume, as shown in SCM experiments (Figs. 4a,b). In addition, a smaller entrainment will also increase the upper-troposphere temperature, not favorable for high cloud formation. On the other hand, a plume with a larger entrainment rate tends to have a

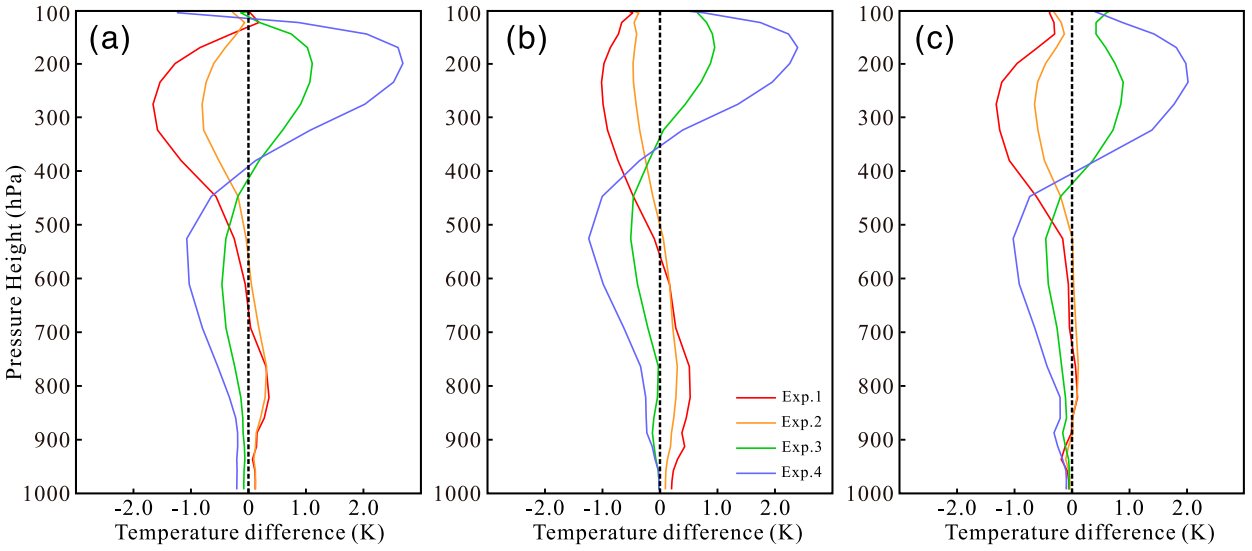

FIG. 14. Vertical profiles of temperature difference between sensitivity tests and CTL over the (a) TIO, (b) WP, and (c) EP.

larger mass flux, favoring more detrainment into the environment, but it can hardly reach the upper troposphere. Therefore, the key is to use a suitable rkm in different environmental regimes to maintain a balance between the plume height and detrainment to achieve the most reasonable cloud distribution and profiles of temperature and moisture. This elucidates the limitations of a plume model with fixed rkm.

The vertical distribution of tropical troposphere temperature (Fig. 16a) and humidity (Fig. 16b) is also significantly regulated by k in the convection scheme, especially at the lower troposphere (600–800 hPa), resulting from the strong evaporation below the plume base. Decreasing k will increase the temperature in the lower troposphere but decrease specific humidity (Fig. 16), leading to decreased relative humidity there. As a result, convection tends to be suppressed due to a warmer and drier lower troposphere above the PBL (large CIN) for a smaller k. Therefore, the energy and mass exchange between lower and upper troposphere is hindered, leading to a colder and drier upper troposphere.

Spatial distribution of precipitation is also slightly changed using various evaporation rates. A larger k slightly increases precipitation in the Philippine Sea and the Bay of Bengal but decreases precipitation near the equator in the Pacific (Fig. 17a). Decreasing k increases precipitation over the tropical Indian Ocean and mideastern Pacific but decreases precipitation over the Bay of Bengal and the Maritime Continent (Fig. 17d).

The TOA net radiation has a small variation with k (Table 3). TOA shortwave radiation tends to increase slightly with

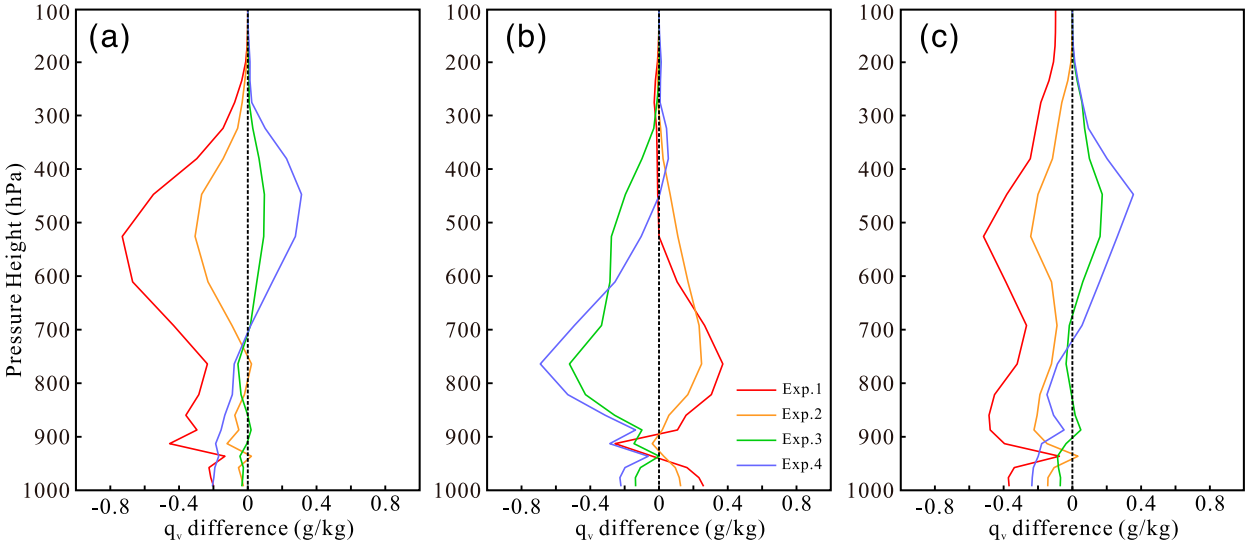

FIG. 15. As in Fig. 14, but for specific humidity.

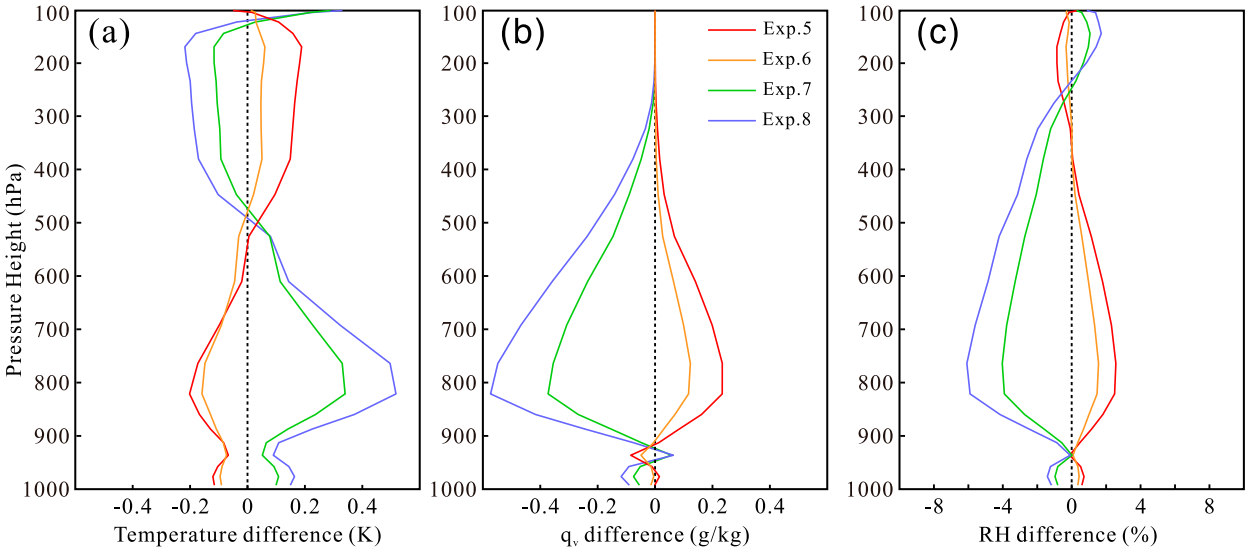

FIG. 16. Vertical profiles of tropical (15°S–15°N) mean (a) temperature, (b) specific humidity, and (c) relative humidity difference between rain evaporation sensitivity tests and CTL.

decreased k, probably related to slightly decreased LWP. TOA longwave radiation also changes with k, with a slightly larger magnitude. Overall, compared with rkm, global mean clouds and radiation do not change much with varying k.

6. Conclusions and discussion

In this study, following Zhao et al. (2018b), a double-plume moist convection scheme was implemented and tested in CAM5. In the scheme, the fractional mixing rate of the deep

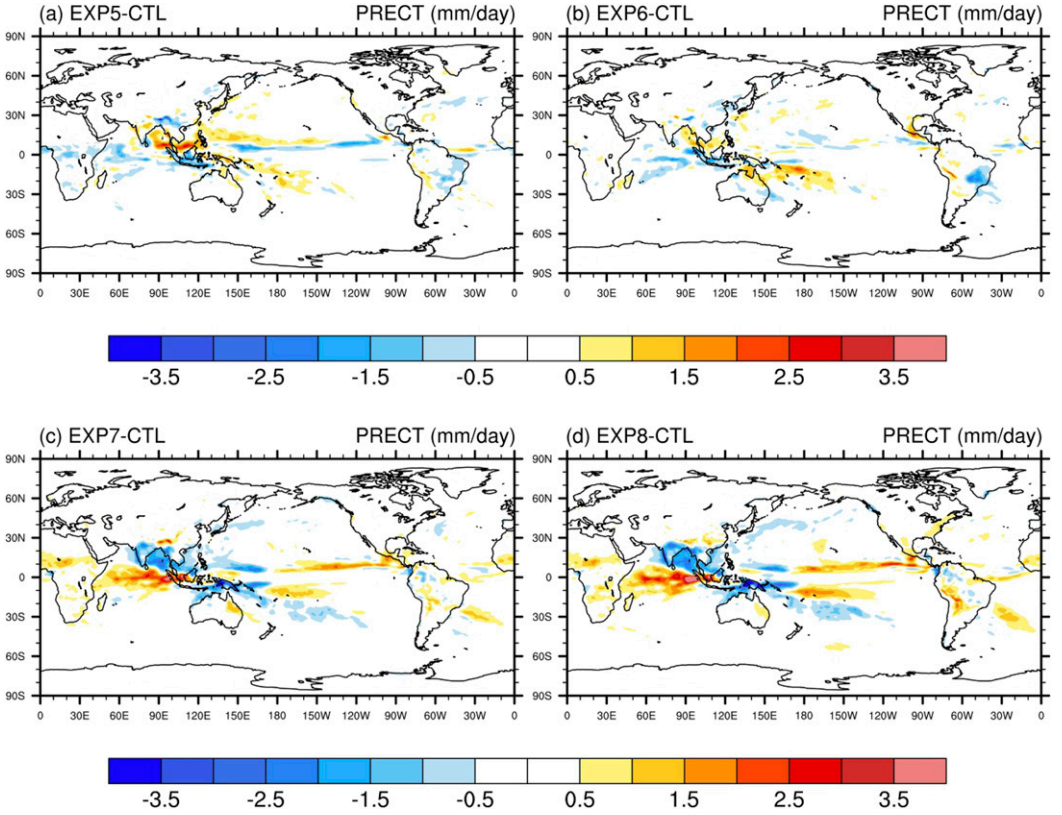

FIG. 17. As in Fig. 13, but between the four rain evaporation sensitivity tests and CTL.

convection is parameterized as a function of environment relative humidity in order to suppress the plume height in dry environments. The relaxed cloud work function closure for deep convection in DP-Z is replaced by a DPCAPE closure (see Table 1). The trigger is also related to the CAPE production instead of the CAPE itself. In addition, source air properties of the plume are set to be the mean environmental properties within the PBL rather than those in a certain layer in order to mimic the turbulent mixing of source air within the PBL.

The scheme was tested in the single-column, short-term hindcast, and AMIP simulations. The scheme performed reasonably well in the TWP-ICE single-column simulations with better cloud profiles. In short-term hindcast simulations, tropical precipitation intensity distribution is largely improved with enhanced magnitude of precipitation diurnal cycle. In AMIP simulations, subtropical marine low clouds and tropical high clouds are better captured using the new scheme. Tropical rainfall is improved over the Indian Ocean, but the changes are mixed over other regions. A series of sensitivity tests by varying the entrainment rates and rain evaporation rates were conducted. Similar to previous studies, entrainment rates can significantly regulate the tropical rainfall and cloud fields, but an optimal entrainment rate is hard to be justified objectively since it might be regime dependent. This indicates that further refinements to parameterization are needed. Future work will be focused on the design of more flexible and environment/regime dependent entrainment rates.

Compared to the conventional moist convection schemes in CAM5, the advantage of the DP-THU scheme is that it represents both deep and shallow scheme in a single unified framework. Namely, both shallow and deep plume share the same cloud model, but using different parameterizations of fractional mixing rate, trigger, and closure. However, there is room for improvement in future. For example, a better coordination with other physical schemes needs to be considered. The double-plume approach works remarkably well in GFDL AM4, but this does not guarantee its performance in CAM5 since the two host models have many differences, such as their boundary layer schemes, cloud microphysics, and macrophysics. Note that the TOA radiation is out of balance by ~7 W m^{-2} using the new scheme, but this could be retuned straightforwardly by altering some key parameters in other schemes, such as the microphysics and macrophysics (e.g., Mauritsen et al. 2012; Hourdin et al. 2017). For example, using a new version of microphysics in CAM5 could reduce the imbalance by ~3 W m^{-2} (not shown). We have not aimed to tune the TOA radiation balance in this study since the scheme will be used with other modifications, such as the PDF cloud macrophysics (Qin et al. 2018) and the single ice microphysics (Zhao et al. 2017) in a GCM recently developed at Tsinghua University based on CESM1.2.1 (Lin et al. 2020).

Acknowledgments. We thank L. Donner for helpful comments on an earlier draft. This work was supported by the National Key Research Project of China (Grant 2018YFC1507001) and the National Natural Science Foundation of China (41921005, 41775098).

Data availability statement. The source code of the scheme and simulations are available at https://doi.org/10.6084/m9.figshare.13667726.

REFERENCES

Acker, J. G., and G. Leptoukh, 2007: Online analysis enhances use of NASA Earth science data. *Eos, Trans. Amer. Geophys. Union*, **88**, 14–17, https://doi.org/10.1029/2007EO020003.

Arakawa, A., 2004: The cumulus parameterization problem: Past, present, and future. *J. Climate*, **17**, 2493–2525, https://doi.org/10.1175/1520-0442(2004)017<2493:RATCPP>2.0.CO;2.

——, and W. H. Schubert, 1974: Interaction of a cumulus cloud ensemble with the large-scale environment, Part I. *J. Atmos. Sci.*, **31**, 674–701, https://doi.org/10.1175/1520-0469(1974)031<0674:IOACCE>2.0.CO;2.

Baba, Y., 2019: Spectral cumulus parameterization based on cloud-resolving model. *Climate Dyn.*, **52**, 309–334, https://doi.org/10.1007/s00382-018-4137-z.

Bacmeister, J. T., M. J. Suarez, and F. R. Robertson, 2006: Rain reevaporation, boundary layer–convection interactions, and Pacific rainfall patterns in an AGCM. *J. Atmos. Sci.*, **63**, 3383–3403, https://doi.org/10.1175/JAS3791.1.

Bechtold, P., J. P. Chaboureau, A. Beljaars, A. K. Betts, M. Köhler, M. Miller, and J. L. Redelsperger, 2004: The simulation of the diurnal cycle of convective precipitation over land in a global model. *Quart. J. Roy. Meteor. Soc.*, **130**, 3119–3137, https://doi.org/10.1256/qj.03.103.

——, M. Köhler, T. Jung, F. Doblas-Reyes, M. Leutbecher, and Coauthors, 2008: Advances in simulating atmospheric variability with the ECMWF model: From synoptic to decadal time-scales. *Quart. J. Roy. Meteor. Soc.*, **134**, 1337–1351, https://doi.org/10.1002/qj.289.

Betts, A. K., and M. J. Miller, 1986: A new convective adjustment scheme. Part II: Single column tests using GATE wave, BOMEX, ATEX and arctic air-mass data sets. *Quart. J. Roy. Meteor. Soc.*, **112**, 693–709, https://doi.org/10.1002/qj.49711247308.

Bodas-Salcedo, A., and Coauthors, 2011: COSP: Satellite simulation software for model assessment. *Bull. Amer. Meteor. Soc.*, **92**, 1023–1043, https://doi.org/10.1175/2011BAMS2856.1.

Bretherton, C. S., and S. Park, 2008: A new bulk shallow-cumulus model and implications for penetrative entrainment feedback on updraft buoyancy. *J. Atmos. Sci.*, **65**, 2174–2193, https://doi.org/10.1175/2007JAS2242.1.

——, and ——, 2009: A new moist turbulence parameterization in the Community Atmosphere Model. *J. Climate*, **22**, 3422–3448, https://doi.org/10.1175/2008JCLI2556.1.

——, J. R. McCaa, and H. Grenier, 2004: A new parameterization for shallow cumulus convection and its application to marine subtropical cloud-topped boundary layers. Part I: Description and 1D results. *Mon. Wea. Rev.*, **132**, 864–882, https://doi.org/10.1175/1520-0493(2004)132<0864:ANPFSC>2.0.CO;2.

Bryan, G. H., and J. M. Fritsch, 2004: A reevaluation of ice–liquid water potential temperature. *Mon. Wea. Rev.*, **132**, 2421–2431, https://doi.org/10.1175/1520-0493(2004)132<2421:AROIWP>2.0.CO;2.

Chepfer, H., S. Bony, D. Winker, G. Cesana, J. L. Dufresne, P. Minnis, C. J. Stubenrauch, and S. Zeng, 2010: The GCM-oriented CALIPSO Cloud Product (CALIPSO-GOCCP).

J. Geophys. Res., **115**, D00H16, https://doi.org/10.1029/2009JD012251.

Cui, Z., G. J. Zhang, Y. Wang, and S. Xie, 2021: Understanding the roles of convective trigger functions in the diurnal cycle of precipitation in the NCAR CAM5. *J. Climate*, **34**, 6473–6489, https://doi.org/10.1175/JCLI-D-20-0699.1.

Dai, A., 2006: Precipitation characteristics in eighteen coupled climate models. *J. Climate*, **19**, 4605–4630, https://doi.org/10.1175/JCLI3884.1.

Derbyshire, S. H., I. Beau, P. Bechtold, J. Y. Grandpeix, J. M. Piriou, J. L. Redelsperger, and P. M. M. Soares, 2004: Sensitivity of moist convection to environmental humidity. *Quart. J. Roy. Meteor. Soc.*, **130**, 3055–3079, https://doi.org/10.1256/qj.03.130.

——, A. V. Maidens, S. F. Milton, R. A. Stratton, and M. R. Willett, 2011: Adaptive detrainment in a convective parameterization. *Quart. J. Roy. Meteor. Soc.*, **137**, 1856–1871, https://doi.org/10.1002/qj.875.

Donner, L. J., 1986: Sensitivity of the thermal balance in a general circulation model to a parameterization for cumulus convection with radiatively interactive clouds. *J. Atmos. Sci.*, **43**, 2277–2288, https://doi.org/10.1175/1520-0469(1986)043<2277:SOTTBI>2.0.CO;2.

Gehne, M., T. M. Hamill, G. N. Kiladis, and K. E. Trenberth, 2016: Comparison of global precipitation estimates across a range of temporal and spatial scales. *J. Climate*, **29**, 7773–7795, https://doi.org/10.1175/JCLI-D-15-0618.1.

Gettelman, A., and H. Morrison, 2015: Advanced two-moment bulk microphysics for global models. Part I: Off-line tests and comparison with other schemes. *J. Climate*, **28**, 1268–1287, https://doi.org/10.1175/JCLI-D-14-00102.1.

Golaz, J., and Coauthors, 2019: The DOE E3SM Coupled Model version 1: Overview and evaluation at standard resolution. *J. Adv. Model. Earth Syst.*, **11**, 2089–2129, https://doi.org/10.1029/2018MS001603.

Gregory, D., 2001: Estimation of entrainment rate in simple models of convective clouds. *Quart. J. Roy. Meteor. Soc.*, **127**, 53–72, https://doi.org/10.1002/qj.49712757104.

Grenier, H., and C. S. Bretherton, 2001: A moist PBL parameterization for large-scale models and its application to subtropical cloud-topped marine boundary layers. *Mon. Wea. Rev.*, **129**, 357–377, https://doi.org/10.1175/1520-0493(2001)129<0357:AMPPFL>2.0.CO;2.

Hannay, C., D. L. Williamson, J. J. Hack, J. T. Kiehl, J. G. Olson, S. A. Klein, C. S. Bretherton, and M. Köhler, 2009: Evaluation of forecasted southeast Pacific stratocumulus in the NCAR, GFDL, and ECMWF models. *J. Climate*, **22**, 2871–2889, https://doi.org/10.1175/2008JCLI2479.1.

Hohenegger, C., and C. S. Bretherton, 2011: Simulating deep convection with a shallow convection scheme. *Atmos. Chem. Phys.*, **11**, 10 389–10 406, https://doi.org/10.5194/acp-11-10389-2011.

Hourdin, F., and Coauthors, 2006: The LMDZ4 general circulation model: Climate performance and sensitivity to parameterized physics with emphasis on tropical convection. *Climate Dyn.*, **27**, 787–813, https://doi.org/10.1007/s00382-006-0158-0.

——, and Coauthors, 2017: The art and science of climate model tuning. *Bull. Amer. Meteor. Soc.*, **98**, 589–602, https://doi.org/10.1175/BAMS-D-15-00135.1.

Huffman, G. J., R. F. Adler, D. T. Bolvin, and G. Gu, 2009: Improving the global precipitation record: GPCP version 2.1. *Geophys. Res. Lett.*, **36**, L17808, https://doi.org/10.1029/2009GL040000.

Jeevanjee, N., 2017: Vertical velocity in the gray zone. *J. Adv. Model. Earth Syst.*, **9**, 2304–2316, https://doi.org/10.1002/2017MS001059.

Kain, J. S., and J. M. Fritsch, 1990: A one-dimensional entraining/detraining plume model and its application in convective parameterization. *J. Atmos. Sci.*, **47**, 2784–2802, https://doi.org/10.1175/1520-0469(1990)047<2784:AODEPM>2.0.CO;2.

Kay, J. E., and Coauthors, 2012: Exposing global cloud biases in the Community Atmosphere Model (CAM) using satellite observations and their corresponding instrument simulators. *J. Climate*, **25**, 5190–5207, https://doi.org/10.1175/JCLI-D-11-00469.1.

Kessler, E., 1969: On the distribution and continuity of water substance in atmospheric circulations. *On the Distribution and Continuity of Water Substance in Atmospheric Circulations, Meteor. Monogr.*, No. 10, Amer. Meteor. Soc., 1–84, https://doi.org/10.1007/978-1-935704-36-2_1.

Khairoutdinov, M. F., and D. A. Randall, 2002: Similarity of deep continental cumulus convection as revealed by a three-dimensional cloud-resolving model. *J. Atmos. Sci.*, **59**, 2550–2566, https://doi.org/10.1175/1520-0469(2002)059<2550:SODCCC>2.0.CO;2.

Knutson, T. R., and R. E. Tuleya, 2004: Impact of CO_2-induced warming on simulated hurricane intensity and precipitation: Sensitivity to the choice of climate model and convective parameterization. *J. Climate*, **17**, 3477–3495, https://doi.org/10.1175/1520-0442(2004)017<3477:IOCWOS>2.0.CO;2.

Kuo, H. L., 1965: On formation and intensification of tropical cyclones through latent heat release by cumulus convection. *J. Atmos. Sci.*, **22**, 40–63, https://doi.org/10.1175/1520-0469(1965)022<0040:OFAIOT>2.0.CO;2.

——, 1974: Further studies of the parameterization of the influence of cumulus convection on large-scale flow. *J. Atmos. Sci.*, **31**, 1232–1240, https://doi.org/10.1175/1520-0469(1974)031<1232:FSOTPO>2.0.CO;2.

Lin, J. L., 2007: The double-ITCZ problem in IPCC AR4 coupled GCMs: Ocean–atmosphere feedback analysis. *J. Climate*, **20**, 4497–4525, https://doi.org/10.1175/JCLI4272.1.

——, and Coauthors, 2006: Tropical intraseasonal variability in 14 IPCC AR4 climate models. Part I: Convective signals. *J. Climate*, **19**, 2665–2690, https://doi.org/10.1175/JCLI3735.1.

Lin, Y., 2019: Impact of cumulus microphysics and entrainment specification on tropical cloud and radiation in GFDL AM2. *Earth Syst. Environ.*, **3**, 255–266, https://doi.org/10.1007/s41748-019-00099-9.

——, and Coauthors, 2012: TWP-ICE global atmospheric model intercomparison: Convection responsiveness and resolution impact. *J. Geophys. Res.*, **117**, D09111, https://doi.org/10.1029/2011JD017018.

——, M. Zhao, Y. Ming, J.-C. Golaz, L. J. Donner, S. A. Klein, V. Ramaswamy, and S. Xie, 2013: Precipitation partitioning, tropical clouds, and intraseasonal variability in GFDL AM2. *J. Climate*, **26**, 5453–5466, https://doi.org/10.1175/JCLI-D-12-00442.1.

——, and Coauthors, 2020: Community Integrated Earth System Model (CIESM): Description and evaluation. *J. Adv. Model. Earth Syst.*, **12**, e2019MS002036, https://doi.org/10.1029/2019MS002036.

Loeb, N. G., B. A. Wielicki, D. R. Doelling, G. L. Smith, D. F. Keyes, S. Kato, N. Manalo-Smith, and T. Wong, 2009: Toward optimal closure of the Earth's top-of-atmosphere radiation budget. *J. Climate*, **22**, 748–766, https://doi.org/10.1175/2008JCLI2637.1.

Lu, C., Y. Liu, S. Niu, and A. M. Vogelmann, 2012: Lateral entrainment rate in shallow cumuli: Dependence on dry air sources and probability density functions. *Geophys. Res. Lett.*, **39**, L20812, https://doi.org/10.1029/2012GL053646.

Ma, H. Y., and Coauthors, 2014: On the correspondence between mean forecast errors and climate errors in CMIP5 models. *J. Climate*, **27**, 1781–1798, https://doi.org/10.1175/JCLI-D-13-00474.1.

——, and Coauthors, 2015: An improved hindcast approach for evaluation and diagnosis of physical processes in global climate models. *J. Adv. Model. Earth Syst.*, **7**, 1810–1827, https://doi.org/10.1002/2015MS000490.

Maher, P., G. K. Vallis, S. C. Sherwood, M. J. Webb, and P. G. Sansom, 2018: The impact of parameterized convection on climatological precipitation in atmospheric global climate models. *Geophys. Res. Lett.*, **45**, 3728–3736, https://doi.org/10.1002/2017GL076826.

Manabe, S., J. Smagorinsky, and R. F. Strickler, 1965: Simulated climatology of a general circulation model with a hydrologic cycle. *Mon. Wea. Rev.*, **93**, 769–798, https://doi.org/10.1175/1520-0493(1965)093<0769:SCOAGC>2.3.CO;2.

Mapes, B. E., 2000: Convective inhibition, subgrid-scale triggering energy, and stratiform instability in a toy tropical wave model. *J. Adv. Model. Earth Syst.*, **57**, 1515–1535, https://doi.org/10.1175/1520-0469(2000)057<1515:CISSTE>2.0.CO;2.

——, and R. Neale, 2011: Parameterizing convective organization to escape the entrainment dilemma. *J. Adv. Model. Earth Syst.*, **3**, M06004, https://doi.org/10.1029/2011MS000042.

Mauritsen, T., and Coauthors, 2012: Tuning the climate of a global model. *J. Adv. Model. Earth Syst.*, **4**, M00A01, https://doi.org/10.1029/2012MS000154.

May, P. T., J. H. Mather, G. Vaughan, C. Jakob, G. M. McFarquhar, K. N. Bower, and G. G. Mace, 2008: The Tropical Warm Pool International Cloud Experiment. *Bull. Amer. Meteor. Soc.*, **89**, 629–646, https://doi.org/10.1175/BAMS-89-5-629.

Moorthi, S., and M. Suarez, 1999: Documentation of version 2 of Relaxed Arakawa-Schubert cumulus parameterization with convective downdrafts. NOAA Tech. Rep. NWS/NCEP 99-01, 44 pp.

Morrison, H., and A. Gettelman, 2008: A new two-moment bulk stratiform cloud microphysics scheme in the Community Atmosphere Model, version 3 (CAM3). Part I: Description and numerical tests. *J. Climate*, **21**, 3642–3659, https://doi.org/10.1175/2008JCLI2105.1.

Neale, R. B., and Coauthors, 2012: Description of the NCAR Community Atmosphere Model (CAM 5.0). NCAR Tech. Note NCAR/TN-486+STR, 289 pp.

Park, S., 2014: A unified convection scheme (UNICON). Part I: Formulation. *J. Atmos. Sci.*, **71**, 3902–3930, https://doi.org/10.1175/JAS-D-13-0233.1.

——, C. S. Bretherton, and P. J. Rasch, 2014: Integrating cloud processes in the Community Atmosphere Model, version 5. *J. Climate*, **27**, 6821–6856, https://doi.org/10.1175/JCLI-D-14-00087.1.

Pendergrass, A. G., and D. L. Hartmann, 2014: Changes in the distribution of rain frequency and intensity in response to global warming. *J. Climate*, **27**, 8372–8383, https://doi.org/10.1175/JCLI-D-14-00183.1.

Phillips, T. J., and Coauthors, 2004: Evaluating parameterizations in general circulation models: Climate simulation meets weather prediction. *Bull. Amer. Meteor. Soc.*, **85**, 1903–1916, https://doi.org/10.1175/BAMS-85-12-1903.

Qin, Y., Y. Lin, S. Xu, H. Y. Ma, and S. Xie, 2018: A diagnostic PDF cloud scheme to improve subtropical low clouds in NCAR Community Atmosphere Model (CAM5). *J. Adv. Model. Earth Syst.*, **10**, 320–341, https://doi.org/10.1002/2017MS001095.

Randall, D. A., K. M. Xu, R. J. Somerville, and S. Iacobellis, 1996: Single-column models and cloud ensemble models as links between observations and climate models. *J. Climate*, **9**, 1683–1697, https://doi.org/10.1175/1520-0442(1996)009<1683:SCMACE>2.0.CO;2.

——, M. Khairoutdinov, A. Arakawa, and W. Grabowski, 2003: Breaking the cloud. Parameterization deadlock. *Bull. Amer. Meteor. Soc.*, **84**, 1547–1564, https://doi.org/10.1175/BAMS-84-11-1547.

Rayner, N. A. A., D. E. Parker, E. B. Horton, C. K. Folland, L. V. Alexander, D. P. Rowell, E. C. Kent, and A. Kaplan, 2003: Global analyses of sea surface temperature, sea ice, and night marine air temperature since the late nineteenth century. *J. Geophys. Res.*, **108**, 4407, https://doi.org/10.1029/2002JD002670.

Riemann-Campe, K., K. Fraedrich, and F. Lunkeit, 2009: Global climatology of convective available potential energy (CAPE) and convective inhibition (CIN) in ERA-40 reanalysis. *Atmos. Res.*, **93**, 534–545, https://doi.org/10.1016/j.atmosres.2008.09.037.

Romps, D. M., 2010: A direct measure of entrainment. *J. Atmos. Sci.*, **67**, 1908–1927, https://doi.org/10.1175/2010JAS3371.1.

——, 2015: MSE minus CAPE is the true conserved variable for an adiabatically lifted parcel. *J. Atmos. Sci.*, **72**, 3639–3646, https://doi.org/10.1175/JAS-D-15-0054.1.

Schmidt, G. A., and Coauthors, 2014: Configuration and assessment of the GISS ModelE2 contributions to the CMIP5 archive. *J. Adv. Model. Earth Syst.*, **6**, 141–184, https://doi.org/10.1002/2013MS000265.

Siebesma, A. P., P. M. Soares, and J. Teixeira, 2007: A combined eddy-diffusivity mass-flux approach for the convective boundary layer. *J. Atmos. Sci.*, **64**, 1230–1248, https://doi.org/10.1175/JAS3888.1.

Slingo, J., and Coauthors, 1994: Mean climate and transience in the tropics of the UGAMP GCM: Sensitivity to convective parameterization. *Quart. J. Roy. Meteor. Soc.*, **120**, 881–922, https://doi.org/10.1002/qj.49712051807.

Stephens, G. L., and Coauthors, 2010: Dreary state of precipitation in global models. *J. Geophys. Res.*, **115**, D24211, https://doi.org/10.1029/2010JD014532.

Stirling, A. J., and R. A. Stratton, 2012: Entrainment processes in the diurnal cycle of deep convection over land. *Quart. J. Roy. Meteor. Soc.*, **138**, 1135–1149, https://doi.org/10.1002/qj.1868.

Sui, C. H., M. Satoh, and K. Suzuki, 2020: Precipitation efficiency and its role in cloud-radiative feedbacks to climate variability. *J. Meteor. Soc. Japan*, **98**, 261–282, https://doi.org/10.2151/jmsj.2020-024.

Sundqvist, H., 1988: Parameterization of condensation and associated clouds in models for weather prediction and general circulation simulation. *Physically-Based Modelling and Simulation of Climate and Climatic Change*, Springer, 433–461.

Tokioka, T., K. Yamazaki, A. Kitoh, and T. Ose, 1988: The equatorial 30-60 day oscillation and the Arakawa-Schubert penetrative cumulus parameterization. *J. Meteor. Soc. Japan*, **66**, 883–901, https://doi.org/10.2151/JMSJ1965.66.6_883.

von Salzen, K., and N. A. McFarlane, 2002: Parameterization of the bulk effects of lateral and cloud-top entrainment in transient shallow cumulus clouds. *J. Atmos. Sci.*, **59**, 1405–1430,

https://doi.org/10.1175/1520-0469(2002)059<1405:POTBEO>2.0.CO;2.

Wagner, T. J., D. D. Turner, L. K. Berg, and S. K. Krueger, 2013: Ground-based remote retrievals of cumulus entrainment rates. *J. Atmos. Oceanic Technol.*, **30**, 1460–1471, https://doi.org/10.1175/JTECH-D-12-00187.1.

Walters, D., and Coauthors, 2019: The Met Office Unified Model global atmosphere 7.0/7.1 and JULES global land 7.0 configurations. *Geosci. Model Dev.*, **12**, 1909–1963, https://doi.org/10.5194/gmd-12-1909-2019.

Wang, X., and M. Zhang, 2013: An analysis of parameterization interactions and sensitivity of single-column model simulations to convection schemes in CAM4 and CAM5. *J. Geophys. Res. Atmos.*, **118**, 8869–8880, https://doi.org/10.1002/jgrd.50690.

Wang, Y., and G. J. Zhang, 2016: Global climate impacts of stochastic deep convection parameterization in the NCAR CAM 5. *J. Adv. Model. Earth Syst.*, **8**, 1641–1656, https://doi.org/10.1002/2016MS000756.

Wang, Y.-C., S. Xie, S. Tang, and W. Lin, 2020: Evaluation of an improved convective triggering function: Observational evidence and SCM tests. *J. Geophys. Res. Atmos.*, **125**, e2019JD031651, https://doi.org/10.1029/2019JD031651.

Xie, S., and M. Zhang, 2000: Impact of the convection triggering function on single-column model simulations. *J. Geophys. Res.*, **105**, 14 983–14 996, https://doi.org/10.1029/2000JD900170.

——, T. Hume, C. Jakob, S. A. Klein, R. B. McCoy, and M. Zhang, 2010: Observed large-scale structures and diabatic heating and drying profiles during TWP-ICE. *J. Climate*, **23**, 57–79, https://doi.org/10.1175/2009JCLI3071.1.

——, H. Y. Ma, J. S. Boyle, S. A. Klein, and Y. Zhang, 2012: On the correspondence between short-and long-time-scale systematic errors in CAM4/CAM5 for the year of tropical convection. *J. Climate*, **25**, 7937–7955, https://doi.org/10.1175/JCLI-D-12-00134.1.

——, and Coauthors, 2019: Improved diurnal cycle of precipitation in E3SM with a revised convective triggering function. *J. Adv. Model. Earth Syst.*, **11**, 2290–2310, https://doi.org/10.1029/2019MS001702.

Yang, B., and Coauthors, 2013: Uncertainty quantification and parameter tuning in the CAM5 Zhang-McFarlane convection scheme and impact of improved convection on the global circulation and climate. *J. Geophys. Res. Atmos.*, **118**, 395–415, https://doi.org/10.1029/2012JD018213.

Yoshimura, H., R. Mizuta, and H. Murakami, 2015: A spectral cumulus parameterization scheme interpolating between two convective updrafts with semi-Lagrangian calculation of transport by compensatory subsidence. *Mon. Wea. Rev.*, **143**, 597–621, https://doi.org/10.1175/MWR-D-14-00068.1.

Yu, H., M. Zhang, W. Lin, and X. Zhang, 2017: Cloud transitions: Comparison of temporal variation in the southeastern Pacific with the spatial variation in the northeastern Pacific at low latitudes. *Int. J. Climatol.*, **37**, 2923–2933, https://doi.org/10.1002/joc.4889.

Zhang, G. J., and N. A. McFarlane, 1995: Sensitivity of climate simulations to the parameterization of cumulus convection in the Canadian Climate Centre general circulation model. *Atmos.–Ocean*, **33**, 407–446, https://doi.org/10.1080/07055900.1995.9649539.

——, and M. Mu, 2005: Effects of modifications to the Zhang-McFarlane convection parameterization on the simulation of the tropical precipitation in the National Center for Atmospheric Research Community Climate Model, version 3. *J. Geophys. Res.*, **110**, D09109, https://doi.org/10.1029/2004JD005617.

Zhang, M., S. Xie, X. Liu, W. Lin, K. Zhang, H.-Y. Ma, X. Zheng, and Y. Zhang, 2020: Toward understanding the simulated phase partitioning of arctic single-layer mixed-phase clouds in E3SM. *Earth Space Sci.*, **7**, e2020EA001125, https://doi.org/10.1029/2020EA001125.

Zhao, C., and Coauthors, 2012: Toward understanding of differences in current cloud retrievals of ARM ground-based measurements. *J. Geophys. Res.*, **117**, D10206, https://doi.org/10.1029/2011JD016792.

Zhao, M., and P. H. Austin, 2005a: Life cycle of numerically simulated shallow cumulus clouds. Part I: Transport. *J. Atmos. Sci.*, **62**, 1269–1290, https://doi.org/10.1175/JAS3414.1.

——, and ——, 2005b: Life cycle of numerically simulated shallow cumulus clouds. Part II: Mixing dynamics. *J. Atmos. Sci.*, **62**, 1291–1310, https://doi.org/10.1175/JAS3415.1.

——, and Coauthors, 2018a: The GFDL global atmosphere and land model AM4.0/LM4.0: 1. Simulation characteristics with prescribed SSTs. *J. Adv. Model. Earth Syst.*, **10**, 691–734, https://doi.org/10.1002/2017MS001208.

——, and Coauthors, 2018b: The GFDL global atmosphere and land model AM4.0/LM4.0: 2. Model description, sensitivity studies, and tuning strategies. *J. Adv. Model. Earth Syst.*, **10**, 735–769, https://doi.org/10.1002/2017MS001209.

Zhao, X., Y. Lin, Y. Peng, B. Wang, H. Morrison, and A. Gettelman, 2017: A single ice approach using varying ice particle properties in global climate model microphysics. *J. Adv. Model. Earth Syst.*, **9**, 2138–2157, https://doi.org/10.1002/2017MS000952.

Zheng, X., S. A. Klein, H. Y. Ma, P. Bogenschutz, A. Gettelman, and V. E. Larson, 2016: Assessment of marine boundary layer cloud simulations in the CAM with CLUBB and updated microphysics scheme based on ARM observations from the Azores. *J. Geophys. Res. Atmos.*, **121**, 8472–8492, https://doi.org/10.1002/2016JD025274.